

The LMDZ4 general circulation model: climate performance and sensitivity to parametrized physics with emphasis on tropical convection

Frédéric Hourdin[‡], Ionela Musat¹, Sandrine Bony¹, Pascale Braconnot², Francis Codron¹, Jean-Louis Dufresne¹, Laurent Fairhead¹, Marie-Angèle Filiberti³, Pierre Friedlingstein², Jean-Yves Grandpeix¹, Gerhard Krinner⁴, Phu LeVan¹, Zhao-Xin Li¹, François Lott¹

¹ *Laboratoire de Météorologie Dynamique du CNRS,*

² *Laboratoire des Sciences du Climat et de l'Environnement,*

³ *Institut Pierre Simon Laplace,*

⁴ *Laboratoire de Glaciologie Géophysique de L'environnement.*

Submitted to *Climate Dynamics*

Draft, May 3, 2005

Abstract

The LMDZ general circulation model is the atmospheric component of the IPSL coupled model IPSL-CM4 which has been used to perform climate change simulations for the 4th IPCC assessment report. During the development phase of the coupled model, the atmospheric model has undergone a series of improvements and tunings which define the LMDZ4 version. The main aspects of the model climatology forced by observed sea surface temperature are documented here. A major improvement with respect to the previous LMDZ3 version concerns the parametrization of tropical convection. The sensitivity of the tropical Hadley-Walker circulation to the parametrization of cumulus convection and clouds is analysed. The tropical circulation is characterized using scalar potentials associated to the horizontal wind and horizontal transport of geopotential (the Laplacian of which is, to a scaling factor, the total vertical momentum in the atmospheric column). The effect of parametrized physics is analysed in a regime sorted framework using the vertical velocity at 500 hPa as a proxy. Compared to Tiedtke's con-

vection scheme, used in the previous version LMDZ3, Emanuel's scheme improves the representation of the Hadley-Walker circulation, with a relatively stronger and deeper convection over tropical continents. The tendency of the model to produce marked patterns of concentrated rainfall over oceans is also a specific signature of the convective closure in moisture convergence used in the previous version. Both the convection and cloud schemes are shown to control the relative importance of large scale convection over land and ocean, an important point for the behavior of the coupled model.

1 Introduction

A great amount of effort has been spent in the past few years by climate modelers to prepare improved climate models suited to climate change simulations, in support of the 4th assessment report of the Intergovernmental Panel on Climate Change (IPCC). Climate change modeling is a particular exercise in that the quality of the model can hardly be assessed with respect to observation. Because of uncertainties in radiative forcing, the observed 20th century climate change does not yet provide a strong constraint on climate sensitivity.

Thus confidence in climate change predictions can

[‡]Corresponding author address: Laboratoire de Météorologie Dynamique, UPMC, Tr 45-55, 3eme et., B99, F-75252 Paris Cedex 05, FRANCE; E-mail : hourdin@lmd.jussieu.fr; Tel : 33-1-44278410; Fax: 33-1-44276272

be improved in two ways: one can either identify some of the mechanisms involved in climate variations over the last decades or in paleoclimates, and then assess the model in terms of those particular mechanisms or one can improve the physical content of the model. A key issue in that last respect is the representation of unresolved subgrid-scale phenomena such as turbulent transport in the planetary boundary layer, convection, clouds and surface processes. All these processes are accounted for in climate models through parametrizations, in which the complexity of the real world is reduced to a few deterministic equations.

Climate change modeling is also a challenge because it requires appropriate treatment not only of the atmospheric physics but also of ocean thermodynamics and circulation, water budget including routing from continental surfaces to the ocean, etc. A full prediction for a given “scenario” of anthropogenic emissions should also include the interactive computation of the evolution of the atmospheric composition, under the effect of bio-geochemical processes for carbon dioxide or chemistry for methane or ozone. With these perspectives in mind, atmospheric general circulation models, developed in the 60s for the purpose of meteorological weather forecast, have continuously evolved, incorporating more physics and additional couplings with other components.

Institut Pierre Simon Laplace (IPSL) is involved in the development of such models. Previous versions of the IPSL Coupled Model have been used to study the Holocene climate-vegetation feedback (Braconnot et al., 1999), feedbacks between climate change and the carbon cycle for the evolution of CO₂ (Dufresne et al., 2002), or for the simulation of secular variability (Li and Conil, 2003).

In the new IPSL coupled model (IPSL-CM4: Marti et al., 2005) the atmospheric, oceanic and land models can now simulate both physics and biogeochemistry. However, the biogeochemistry part was not activated in the set of climate change simulations produced for IPCC.

The atmospheric model at the basis of this work, LMDZ4, is presented here. The hydrodynamical core is issued from a rewriting of a general circulation model developed in the 70s (Sadourny and Laval, 1984). The physics package has evolved through time, with a certain continuity with respect to the previous model (Le Treut and Li, 1991; Harzallah and Sadourny, 1994; Li, 1999). The model was also endowed with numerical schemes for the advection of tracers (Hourdin and Armengaud, 1999) and coupled to a scheme for sulfur chemistry (Boucher and Pham, 2002) and tropospheric

chemistry of greenhouse gases (Hauglustaine et al., 2004).

During the development phase of the IPSL-CM4 model, the physics package has undergone major changes with respect to the previous LMDZ3 version. The major change concerns the representation of cumulus convection. The Emanuel (1993) scheme has been preferred to the Tiedtke (1989) scheme as it results in a better spatial distribution of the simulated tropical rainfall. Both the convection and clouds schemes are shown to result in profound changes in the large scale circulation in the tropics and ocean/continent contrasts. Those changes are analysed, based on a series of sensitivity experiments, using (i) velocity potentials (as well as the potential associated to the horizontal transport of geopotential) to characterize the large scale circulation and (ii) a regime-sorted framework (Bony et al., 2004) to analyse the role of physical parametrizations.

First we present the major model improvements and tunings (section 2) and document some aspects of the simulated climate (section 3). Then we analyse in more details the sensitivity of the simulated climate to the parametrized physics with a focus on tropical convection and divergent circulation (section 4). This paper also aims to serve as a reference for the climate studies conducted with the LMDZ model. A companion paper will be dedicated to the coupled model and IPCC simulations.

2 Model description

2.1 LMDZ

LMDZ is the second generation of a climate model developed for about thirty years at Laboratoire de Météorologie Dynamique (Sadourny and Laval, 1984). This model has been used for a number of climate studies (Le Treut et al., 1994; Le Treut et al., 1998). Compared to this old model, the coding of LMDZ is more modular and flexible. The horizontal grid is also stretchable in both longitude and latitude (Z of LMDZ standing for Zoom capability). The physics package has undergone continuous modifications throughout the years. LMDZ is currently used for climate studies at regional (Krinner and Genthon, 1998; Genthon et al., 2002; Zhou and Li, 2002; Poutou et al., 2004; Krinner et al., 2004) and global scales (Li, 1999; Li and Conil, 2003) and for the simulation of the atmospheric transport of trace species (Hourdin and Issartel, 2000; Krinner and Genthon, 2003; Cosme et al., 2005). The last version, LMDZ4, is the result of significant improvements in the physics

package concerning especially cumulus convection, cloud scheme and fine tuning for preparation of the IPSL-CM4 coupled model. LMDZ4 can also be run with an arbitrary number of trace species (Hourdin and Armengaud, 1999) and is coupled to a module of atmospheric chemistry and aerosols (Hauglustaine et al., 2004).

2.2 The dynamical core

The dynamical part of the code is based on a finite-difference formulation of the primitive equations of meteorology (see *e. g.* Sadourny and Laval, 1984). The dynamical equations are discretized on the sphere in a staggered and stretchable longitude-latitude Arakawa C-grid (see *e. g.* Kasahara, 1977). Scalar variables (pressure, temperature, vapour and liquid water as well as tracers) are defined at the center of grid cells whereas wind components are defined at grid cell interfaces. The discretization ensures numerical conservation of both enstrophy (square of the wind rotational) for barotropic flows (according to the schemes originally proposed by Sadourny, 1975b,a) and angular momentum for the axisymmetric component. The time step is bounded by a CFL criterion on the fastest gravity modes. For the applications presented here, with a regular grid of 96 points in longitude and 72 in latitude, the time-step is 3 minutes. For latitudes poleward of 60 degrees in both hemispheres, a longitudinal filter is applied in order to limit the effective resolution to the one at 60 degrees. The time integration is done using a leapfrog scheme, with a periodic predictor/corrector time-step. Both vapour and liquid water are advected with a monotonic second order finite volume scheme (Van Leer, 1977; Hourdin and Armengaud, 1999).

The numerical stability of the model is ensured by the introduction of a horizontal dissipation operator which accounts for the nonlinear interaction between scales explicitly resolved by the grid and motions occurring at sub-grid scales. By conserving enstrophy, the finite-difference formulation correctly represents the vorticity transfer from large to small scales of motions, down to grid-scale cut-off. Without dissipation, enstrophy would accumulate at small scales and eventually produce numerical instabilities. The dissipation operator is based on an iterated Laplacian, designed so as to represent properly the pumping of enstrophy at the scale of the grid.

On the vertical, the model uses a classical hybrid $\sigma - p$ coordinate : the pressure P_l in layer l is defined as a function of surface pressure P_s as

$$P_l = A_l P_s + B_l \quad (1)$$

The values of A_l and B_l are chosen in such a way that the $A_l P_s$ part dominates near the surface (where A_l reaches 1), so that the coordinate follows the surface topography (like so-called σ coordinates), and B_l dominates above several km, making the coordinate equivalent to a pressure coordinate there. The standard version is based on 19 layers. As an example, the averaged pressure levels over the oceans in the tropics are 1004, 985, 956, 914, 852, 770, 667, 547, 422, 311, 233, 183, 140, 104, 72, 47, 27, 14 and 3 hPa. Note that a 50-layer version is also being developed with a specific focus on the stratosphere (Lott et al., submitted to Climate Dynamics).

This dynamical core has been widely used not only for simulations of the Earth atmosphere but also for the numerical simulation of the general circulation of other planetary atmospheres, in particular for Mars (Hourdin et al., 1993; Forget et al., 1999; Levrard et al., 2004) and Titan (Hourdin et al., 1995; Rannou et al., 2002).

2.3 The physics package

Coupled to the dynamical core, the model includes a complete set of physical parametrizations.

The radiation scheme is the one introduced several years ago in the model of the European Centre for Medium-Range Weather Forecasts (ECMWF) by Morcrette: the solar part is a refined version of the scheme developed by Fouquart and Bonnel (1980) and the thermal infra-red part is due to Morcrette et al. (1986). The radiative active species are H_2O , O_3 , CO_2 , O_2 , N_2O , CH_4 , NO_2 and CFCs. The direct and first indirect radiative effect of sulfate aerosols have been introduced in LMDZ (Boucher and Pham, 2002) and compared with observations (Quaas et al., 2004). However, those effects are not activated here and will not be discussed.

Turbulent transport in the planetary boundary layer is treated as a vertical diffusion with an eddy diffusivity K_z which depends on the local Richardson number according to Laval et al. (1981). Upgradient transport of heat in the convective boundary layer is ensured by adding a prescribed countergradient of -1 K km^{-1} to the vertical derivative of potential temperature (Deardorff, 1966). Unstable profiles are prevented using a dry convective adjustment. The surface boundary layer is treated according to Louis (1979a).

Condensation is parametrized separately for convective and non-convective clouds. Parametrizations of moist convection and clouds have undergone large changes in the recent past and are described in specific sections below.

The effects of mountains (drag, lift, gravity waves)

are accounted for using state-of-the-art schemes (Lott and Miller, 1997; Lott, 1999).

The dynamics and physics of the model are clearly separated in the code and communicate through a well defined interface. The dynamical core is written in a 3D world whereas the physics package is coded as a juxtaposition of independent 1D columns. Thus testing the physics package in a single-column context or developing simple climate models in a latitude-altitude frame (Hourdin et al., 2004) are easily done. The physical parametrization equations could also be solved on a spatial grid different from the one of the dynamical core. This allows for instance to "delocalize" the atmospheric physics on the grid of an oceanic model as experienced several years ago by Vintzileos et al. (1999). This clear interface between physics and dynamics is also very important when developing parallel versions for the Earth and other planetary atmospheres.

2.4 Recent improvements

Parametrization of cumulus convection

In the original LMD model, the moist convective adjustment by Manabe et al. (1965) and a modified version of Kuo (1965) were applied sequentially. Motivated in part by the inclusion of the tracer components, the Tiedtke (1989) scheme was chosen for the first versions of the LMDZ model. It was finally replaced by the Emanuel (1993) scheme in the coupled model, which improved significantly the large scale distribution of tropical precipitation as discussed later in the paper.

Tiedtke's and Emanuel's schemes both belong to the category of "mass flux schemes". They attempt to parametrize explicitly the convective mass fluxes (saturated in the convective clouds and unsaturated in the precipitating downdraughts) as well as the induced motions in the environmental air.

In the **Tiedtke scheme** only one convective cloud is considered, comprising one single saturated updraught. Entrainment and detrainment between the cloud and the environment can take place at any level between the free convection level and the free sinking level. There is also one single unsaturated downdraught. The version of Tiedtke's scheme used here is close to the original formulation and relies on a closure in moisture convergence. It presents some systematic defects. One is a systematic overestimate of precipitation over tropical oceans, in particular on the west side of the Indian and Pacific Ocean basins; another is the drastic underestimate of the precipitation during the rainy season over Africa and South America.

One should note that, like all schemes using a moisture convergence closure, this scheme allows for conditional instability of the second kind (CISK). This ability, which has been criticized by Emanuel and others (e.g. Emanuel, 1991; Emanuel et al., 1994), might contribute to the tendency of the simulated convection to occur in intense patches.

In **Emanuel's scheme** the convective clouds are represented by multiple buoyancy sorted saturated draughts (both ascending and descending). The backbones of the convective clouds are regions of adiabatic ascent originating from some low-level layer and ending at their level of neutral buoyancy (*LNB*). Shedding from these adiabatic ascents yields, at each level, a set of draughts which are mixtures of adiabatic ascent air (from which some precipitation is removed) and environmental air. These mixed draughts move adiabatically up or down to levels where, after further removal of precipitation and evaporation of cloudy water, they are at rest at their new levels of neutral buoyancy. Similarly to Tiedtke's scheme, there is one single unsaturated downdraught. It is parametrized with an entraining plume model driven by the evaporation of precipitation. The version of Emanuel's scheme used here is derived from a code delivered by K. Emanuel in 1995, which implements a model very similar to Emanuel (1993) model (note that there are two other published versions: Emanuel (1991); Emanuel and Zivkovic-Rothman (1999)). Our version differs from Emanuel's in the removal of most explicit grid dependencies (e.g. lifting condensation level varies continuously and not from grid level to grid level), which yields a smoother variation of convection intensity with time and a weaker dependence on vertical resolution.

The design of Emanuel's convection scheme is different from most others. Especially, three features make it very different from Tiedtke's scheme:

- Closure and triggering take into account in a crude way both tropospheric instability and convective inhibition. More precisely, the mass flux M_B at cloud base is expressed as:

$$M_B = \alpha B^2 \int_{LNB}^{LFC} \sqrt{CAPE_{(p)}} dp$$

where *LFC* is the level of free convection, *B* is the buoyancy of adiabatically lifted parcels at 40hPa above *LCL*, and $CAPE_{(p)}$ is the work of buoyancy forces between *LFC* and level *p*. α is a scale factor. Inhibition is accounted for by the *B* term and tropospheric instability by the *CAPE* term. As a result, this scheme is not CISK-able, a feature which may have some importance

in the differences between the ITCZ simulated with the two schemes (narrower and sharper with Tiedtke’s scheme).

- Emanuel’s scheme is one of the few schemes simulating precipitating downdraughts with an intensity comparable to the one obtained in CRM simulations (Guichard et al., 2004). This is important for the distribution of water vapour in the troposphere. It is one of the main causes of the difference between convective moistening simulated by Emanuel’s and Tiedtke’s schemes. It is also the reason why convection intensity with Emanuel’s scheme cannot reach as high values as with Tiedtke’s scheme.
- The last feature is a drawback of Emanuel’s scheme: cloud top is always at LNB . As a consequence, a dry free troposphere cannot inhibit deep convection even though it may reduce convection intensity (through entrainment). This lack of sensitivity has consequences for the diurnal cycle of convection over continents and for the modulation of tropical convection by dry intrusions.

Stratiform clouds

As in several other GCMs, the cloud cover f and cloud water content \overline{q}_c are deduced from the large scale total (vapour + condensed) water \overline{q}_t and moisture at saturation, q_{sat} , using a Probability Distribution Function (PDF) $P(q_t)$ for the subgrid-scale total water q_t :

$$f = \int_{q_{\text{sat}}}^{\infty} P(q_t) dq_t \quad \text{and} \quad \overline{q}_c = \int_{q_{\text{sat}}}^{\infty} (q_t - q_{\text{sat}}) P(q_t) dq_t \quad (2)$$

In the original formulation (Le Treut and Li, 1991), the subgrid scale distribution of total water is described by a top hat distribution of width $\sigma = r\overline{q}_t$ around \overline{q}_t , where the ratio r is an imposed parameter (a decreasing function of pressure in LMDZ).

Following Bony and Emmanuel (2001), the top-hat function has recently been replaced by a generalized log-normal function defined on the positive axis. The distribution also depends on one single width parameter. The distribution tends to a Gaussian distribution when the ratio $r = \sigma/\overline{q}_t$ tends to zero. When r increases, because the distribution domain is bounded by 0, the distribution displays an increasing positive skewness, with a tail extending toward large values of q_t . This is consistent with the observation that strong convection is associated with both a large

dispersion of humidities and a large skewness (Xu and Randall, 1996a).

This subgrid-scale distribution is used to predict ”stratiform” (in the sense that they are predicted directly from large scale variables) clouds by using an imposed vertical profile for the ratio r of the form $r_{\text{bot}} + \min((p - p_s)/(p_{\text{top}} - p_s), 1) \times (r_{\text{top}} - r_{\text{bot}})$. For the standard version we use $r_{\text{bot}} = 0.05$, $r_{\text{top}} = 0.33$ and $p_{\text{top}} = 300$ hPa. The predicted clouds precipitate. Reevaporation in the layers below is also computed.

Cloud microphysical properties are computed as described in Bony and Emanuel (2001, Table 2 for water clouds and case ”ICE-OPT” of Table 3 for ice clouds): temperature thresholds (-15°C and 0°C) are used to partition the cloud condensate into liquid and frozen cloud water mixing ratios; cloud optical thickness is computed by using an effective radius of cloud particles set to a constant value for liquid water clouds ($12 \mu\text{m}$ in the simulations presented here), and decreasing with decreasing temperature (from 60 to $3.5 \mu\text{m}$) for ice clouds. The vertical overlap of cloud layers is assumed to be maximum-random.

Convective clouds

Even with these PDFs, the parametrization with a unique function r of pressure is not sufficient to realistically predict the contrast between strongly convective clouds in a rather dry troposphere and more homogeneous conditions. However, large scale relative humidity is not a good predictor of cloud fraction in convective regions (Xu and Randall, 1996b). A special treatment is thus needed to make the parametrization of clouds associated with cumulus convection more closely coupled to the convective activity.

In an early version of the model based on Tiedtke’s scheme, the convective cloud cover was imposed as a function of the total convective rainfall at the surface (Slingo, 1987). For the simulations presented here, this approach is refined by using as a predictor the opposite of the vertical integral of the negative tendency of total water, associated to convection, in place of the surface rainfall. Both predictors are identical for strongly precipitating systems. However, the second formulation results in a much more realistic cloud cover in regions with non precipitating convection as in the trade-winds. This additional tuning has a strong positive impact on cloud radiative forcing over oceans.

For Emanuel’s scheme, we adopt a more consistent approach proposed by Bony and Emmanuel (2001). In this approach, r is estimated in each convective grid cell and at each vertical level from an inverse procedure, so that the in-cloud water content predicted by the

statistical cloud scheme equals the condensed water content predicted by the convective scheme.

Finally the total cloud cover seen by the radiative code is the maximum of the convective and stratiform cloud cover.

Tuning of the boundary layer scheme

The boundary layer scheme is very important for climate and coupling to continental surfaces and oceans. Although some new developments are performed on the parametrization of the boundary layer dynamics (Hourdin et al., 2002), it was decided not to modify too much the old scheme but rather to perform ad-hoc tunings.

The formulation of the boundary layer is very sensitive to a (constant) minimum diffusion coefficient. Specific care was taken in estimating this threshold in order to get the right strength for the polar inversion following the work done by Krinner et al. (1997) and Grenier et al. (2000). It was also shown in the previous version of the LMD model, that this simple tuning was necessary to get the right temperature profiles over sea-ice (Braconnot, 1998).

A different tuning is done on oceans in order to obtain a satisfactory contrast between trade wind cumuli and strato-cumuli on the eastern borders of basins. The diffusion coefficient K_z is first computed with a very small minimum diffusivity (different from the value used on continents and sea ice). If used alone, this diffusivity would produce a strong overestimation of boundary layer cloud coverage over the oceans (Grenier, personal communication). A second diffusivity is then computed conditionally, depending on the strength of the inversion at the boundary layer top. The first coefficient is in fact really used in the regions of strong inversion only (in particular in the strong subsidence on the east side of oceanic basins). In the other areas, the boundary layer scheme is more diffuse at the boundary layer top, producing smaller cloud covers, as observed in the trade wind cumuli.

The formulation of the drag coefficient over the ocean was also revised. In its original version, the surface roughness length over the ocean followed Charnock's formula. The neutral drag coefficient was prescribed to 10^{-3} . The stability functions were those of Louis (1979b). Under unstable conditions over the ocean, the empirical interpolation of Miller et al. (1992) was used between the free convection limit and the neutral approximation.

In the new version, the formulation of Smith (1988) is introduced to compute the surface roughness length. For practical reasons, the differentiation between

heat and momentum drag coefficient is achieved by prescribing a 0.8 factor between the respective neutral drag coefficients, which roughly mimics the difference in Smith (1988) neutral drag coefficient between heat and momentum in moderate to high wind speed. Several sensitivity experiments showed that this factor is important in controlling the evaporation in the subtropics and the advection of moisture in the low level branch of the Hadley circulation. Precipitation over the Pacific warm pool is also sensitive to this parameter.

Surface processes

For coupling purposes, a fractional land-sea mask is introduced in the model (see Appendix A). Each grid box is divided into 4 sub-surfaces corresponding to continental surface, free ocean, sea-ice and ice-sheet. Surface fluxes are computed using parameters (roughness length, albedo, temperature, humidity etc..) adapted to each surface type. For each atmospheric column, vertical diffusion is applied independently for each subsurface, and the resulting tendencies are averaged. In addition, an interface model is also introduced to clearly disconnect surface processes from the atmosphere. The calculation of surface fluxes is done in an independent model, which requires providing this model with the sensitivity of the flux to temperature, in order to preserve the properties of the implicit scheme. With this formulation the flux model can be either a routine in the atmospheric model, an ocean model or a land surface scheme.

For continental surfaces, LMDZ was initially coupled to a very simple thermodynamical model. Thermal conduction below the surface was computed with a 11-layer model following (Hourdin et al., 1993) and soil moisture and evaporation were computed with a bucket model. In this latter, the soil water content is described as a single reservoir height h which evolves according to the net water budget $P - E$ (Precipitation minus Evaporation). $E = \beta E_p$ where E_p is the potential evaporation (that of a free surface of water) and $\beta = \min(1, h/h_p)$ with $h_p = 75$ mm. Water in excess of the maximum content ($h_{\max} = 150$ mm) is lost through run-off.

LMDZ4 is now coupled to the ORCHIDEE surface-vegetation-atmosphere transfer and dynamic vegetation model (de Rosnay et al., 2002; Krinner et al., 2005). ORCHIDEE can be used with a simplified two-layer hydrological scheme (Jacquart and Choissnel, 1995) or a multi-layer formulation of soil humidity transfer (de Rosnay and Polcher, 1998). In the simulations presented here, the two-layer version is used and vegetation distribution is prescribed. Seasonally varying plant leaf area index (LAI) is prescribed after satellite data

(Myneni et al., 2002). As described in Krinner et al. (2005), ORCHIDEE uses the formulation of Ball et al. (1987) for stomatal conductance and of Farquhar et al. (1980) and Collatz et al. (1992) for C3 and C4 plants photosynthesis, respectively. This ensures consistency between the treatment of the hydrological processes, in particular transpiration, and the treatment of stomatal conductance and photosynthesis. Soil temperature is calculated as in Hourdin et al. (1993).

3 Basic elements of model climatology

In this section, we present elements of climatology of the LMDZ4 model using simulations which follow the AMIP II protocol. We first describe the design of these simulations and then discuss the model climatology.

3.1 AMIP simulations

We performed an ensemble of inter-annual simulations following the protocol proposed for the AMIP II experiments. The sea surface temperatures and sea-ice boundary conditions used to force these runs are the monthly mean values constructed at PCMDI (Taylor et al., 2000). These monthly values are first horizontally interpolated on the LMDZ grid and then extrapolated to daily values using cubic-splines.

The AMIP II experimental protocol requirements are all fulfilled for the simulations presented here, the one exception concerning the fact that the model was not explicitly spun-up at the beginning of the AMIP period. Indeed, all of the simulations start from a "quasi-equilibrium" state corresponding to a previous AMIP II simulation for which there were no perceptible trends in deep soil temperature and moisture.

Additional AMIPII recommendations are fulfilled with respect to the CH₄ and N₂O concentrations and the specification of the land-sea mask and topography. The other AMIPII recommendations are not strictly fulfilled. Details of particular treatments or choices are given below. The radiative forcings due to halocarbon concentrations are interactively calculated using 280 ppt for CFC₁₁ and 484 ppt for CFC₁₂. The radiative forcing by sulfate aerosols is not activated in the AMIP runs. The LMDZ model still uses a 360 days calendar. The ozone climatology is based on an analytic formula which fits the Krueger and Mintzner (1976) profile, as well as the variations with altitude and latitude of the maximum ozone concentrations and the total column ozone concentration of Keating and Young (1986). The atmospheric mass and topography are not prescribed

to observed global average values but are quite close to the observed values. In the simulations presented here the global average for the surface pressure is 985.32 hPa (versus 982.4 hPa in the observations) and that of the topographic height is 229.70 m (versus 237.33 m in the observations).

Following the AMIP II protocol and the specifications above, we performed an ensemble of 6 AMIP simulations covering the 1979-2002 period. Each of these simulations differs from the other only by the initial state of the atmosphere, which is issued from 6 different 1st January of a previous AMIP II experiment. For the analyses below, we use either one particular simulation when the model climatology is analysed or the ensemble of simulations when the inter-annual variability is explored. The AMIP simulations are performed with a rather coarse resolution (96×72×19) with respect to current standards. This resolution was chosen in order to be compatible with the realisation of the climate change simulations for IPCC on the computers available to us.

3.2 Mean meridional structure

Fig. 1 presents, in latitude/pressure coordinates, the zonally averaged zonal wind, temperature and relative humidity for average January and July conditions (gray scales). The thick superimposed contours show the difference with the ECMWF ERA40 reanalyses for the same period.

First, and contrary to previous versions of the LMD model, LMDZ4 no longer shows a systematic cold bias in the lower troposphere. A significant cold bias however persists between 100 and 300 hPa at high latitudes. This cold bias is a classical feature of a number of climate models and the reason for it does not seem to have been firmly established yet. For the relative humidity (middle panels of Fig. 1) the agreement with ERA40 seems reasonable with errors generally smaller than 15% and no systematic bias. The intensity of the winter jets is generally somewhat overestimated (lower panels). The summer jets maximum intensity is better reproduced but the jet is globally shifted toward the equator. This shift is seen from the dipolar structure in the difference AMIP-ERA40 with positive difference equatorward and negative difference poleward of the jet.

Some additional diagnostics more specific of low, mid or high latitudes are detailed below.

3.3 Tropics

Regarding the tropics, we show in Fig. 2 the structure of the rainfall and net cloud radiative forcing.

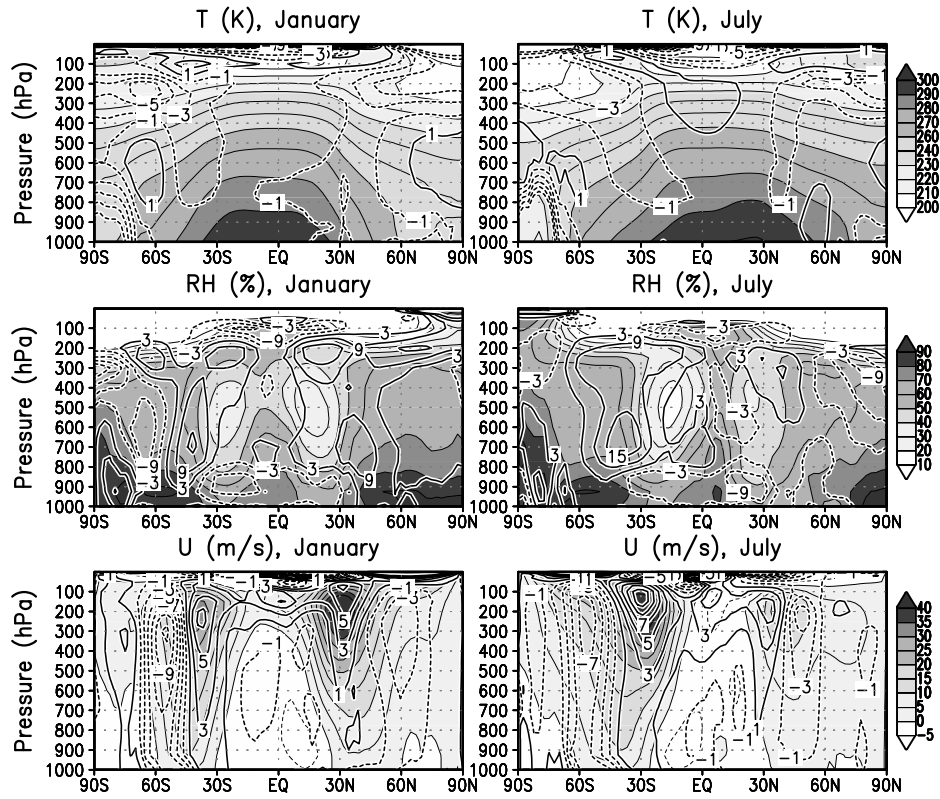
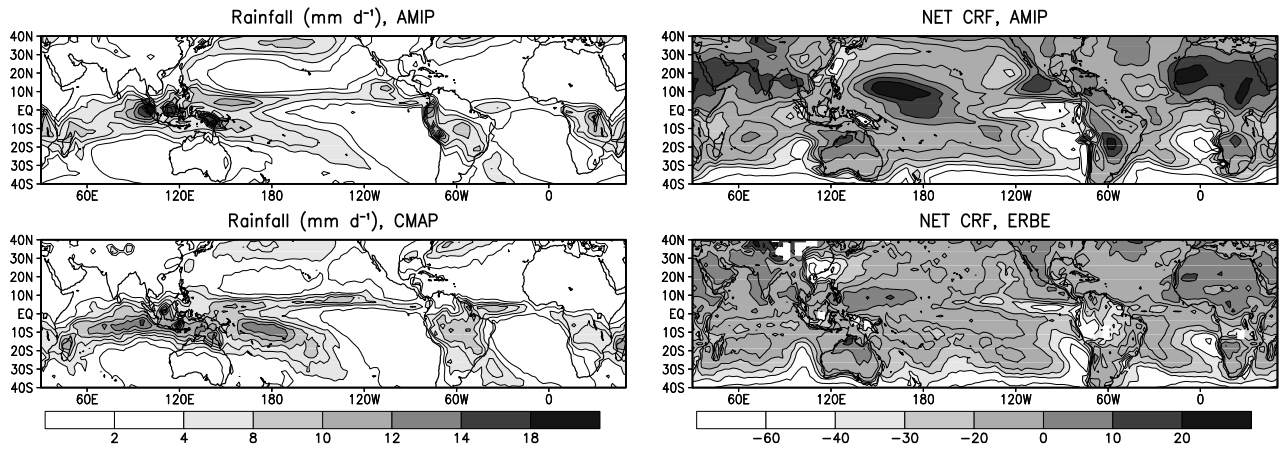


Figure 1: Zonally averaged temperature (T , K), relative humidity (RH , %) and zonal wind (U , m s^{-1}) simulated for the AMIP period (gray scale) in January (left) and July (right). The difference with the ERA40 reanalysis is superimposed with regular (thick) contours (2 K for T , 6% for RH and 2 m s^{-1} for U).

January



July

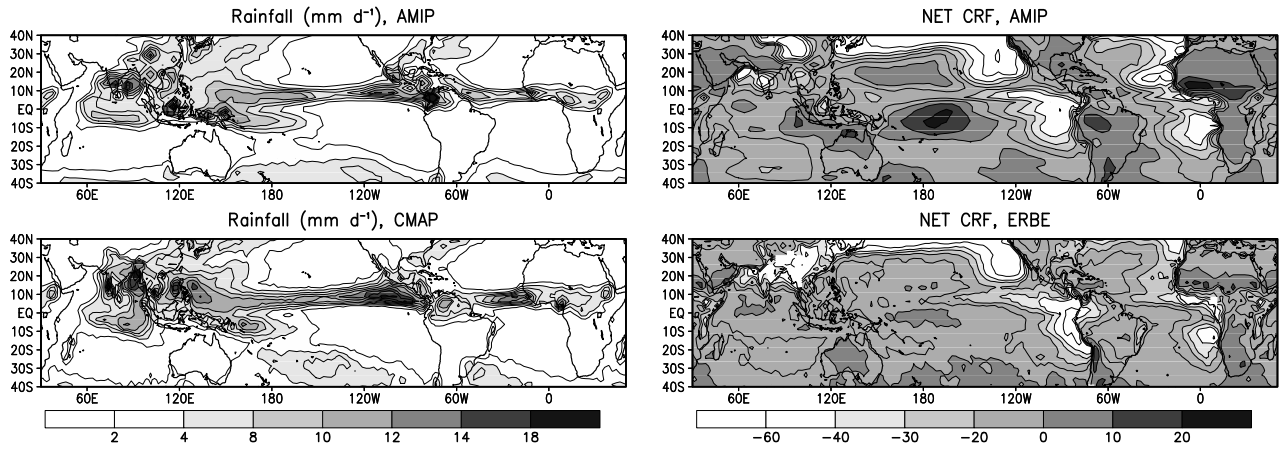


Figure 2: Averaged precipitation (mm/d) and net cloud radiative forcing (W m^{-2}) for the AMIP simulations and for the CMAP and ERBE observations.

The distribution of tropical rainfall (left panels) is reproduced rather well for both July and January. The ITCZ over the Pacific Ocean is probably somewhat too weak in the center of the basin. The maximum rainfall is clearly located on the Indonesia oceanic continent in January. Over continents, the maximum rainfall is also rather well simulated but there is a tendency in the model to "confine" the precipitation regions. This is the case over the amazonian delta for January and over Sahel and North-West India for July. The rainfall monsoon is also underestimated on the West coast of India and overestimated over the indian sub-continent. The maximum over Bay of Bengal almost has the good intensity but it is shifted to the south when compared to CMAP data (Xie and Arkin, 1997) .

The distribution of the net cloud radiative forcing is compared to ERBE (Barkstrom, 1984) on the right panels of Fig. 2. The strong positive bias on the West tropical Pacific Ocean in the winter hemisphere and over Sahara is due to an overestimation of the longwave radiative forcing by high clouds. The negative radiative forcing is also not strong enough over the regions of tropical rainfall on continents, due to an underestimation of the shortwave cloud radiative forcing. However, this bias is partly explained over South America by the underestimation of the convective activity itself (and associated rainfall). This bias is also much larger when the coupling with Bony and Emmanuel (2001) scheme for clouds is not activated (results not shown). However, the net radiative forcing is globally reproduced reasonably well. One can notice in particular a good representation of the seasonal cycle of cloud forcing (by strato-cumulus clouds) on the East side of oceanic basins (with a maximum in local summer) and a good longitudinal contrast over oceans (especially for the summer hemisphere).

3.4 Mid latitudes

Steady and transient planetary waves

For conciseness, and because the variability is largest during winter months, we focus here on first and second order diagnostics during December-January-February for the Northern Hemisphere and June-July-August for the Southern Hemisphere.

For the Northern Hemisphere, the averaged geopotential at 700 hPa, Z700 (Fig. 3, panels a), presents two major troughs at the East coasts of America and Asia, and two major ridges over Northeastern America and Northeastern Europe. There is a less pronounced trough over Central Europe and a weak ridge to its East (i.e. to the North of the Himalayan plateau). These

features are well predicted in the model (left side of Fig. 3) when compared to the reanalysis (right side). This, in part, results from the action at low level of the Subgrid Scale Orographic scheme (Lott, 1999). The model however slightly overestimates the ridge over the Rockies but underestimates the diffluence of the jet over western Europe. The systematic shift of the simulated jets toward the equator is also visible on those maps.

The root mean square of Z700 in Fig 3b reveals two centers of action, slightly to the west of the two major ridges in Fig. 3a. The location of these two centers of action is realistic when compared to reanalysis. The model nevertheless seems to slightly overestimate the tropospheric variability over the North eastern Pacific. As the total variance in the atmosphere is dominated by the low-frequency variability (Sawyer, 1976; Blackmon, 1976), the RMS fields in (panels b) hide the transient eddies resulting from the baroclinic instabilities generated where the midlatitude jet is intense (on the lee side of the two major troughs in panels a). To isolate these baroclinic eddies, we next use the procedure of Hoskins et al. (1996) and define the high pass transient fields by the difference between the daily field and the centered box-car 3-day mean of that field. The RMS of this high pass field is presented in Fig. 3c, for the winter NH. The baroclinic storm tracks are located at the two jet exits, with maximum variance over the western half of the two oceans and extension over the entire oceanic basins. Note nevertheless that over the entire Pacific the model underestimates substantially the high pass RMS.

For the Southern Hemisphere winter, the climatological mean flow (Fig. 3d) is much more zonal. At southern latitudes around 60°S, it presents enhanced variance over near half the globe in latitude, with a maximum over southern east Pacific near the Drake passage (Fig. 3e). The pattern of high frequency in Fig. 3f presents enhanced variance slightly to the north of the maximum of total variance in Fig. 3e. It covers more than half the globe around 50°S. Again, these patterns are rather realistic, with the model overestimating the total variance and underestimating the high pass variance.

Interannual variability

A large number of spatial patterns and indices has emerged in studies of the northern hemisphere winter-time extratropical variability. Recently, Quadrelli and Wallace (2004) have shown that they can all be almost fully retrieved by a linear combination of only two basis patterns: the leading two EOF of the monthly sea level pressure (SLP) field.

The two EOFs computed by a principal component

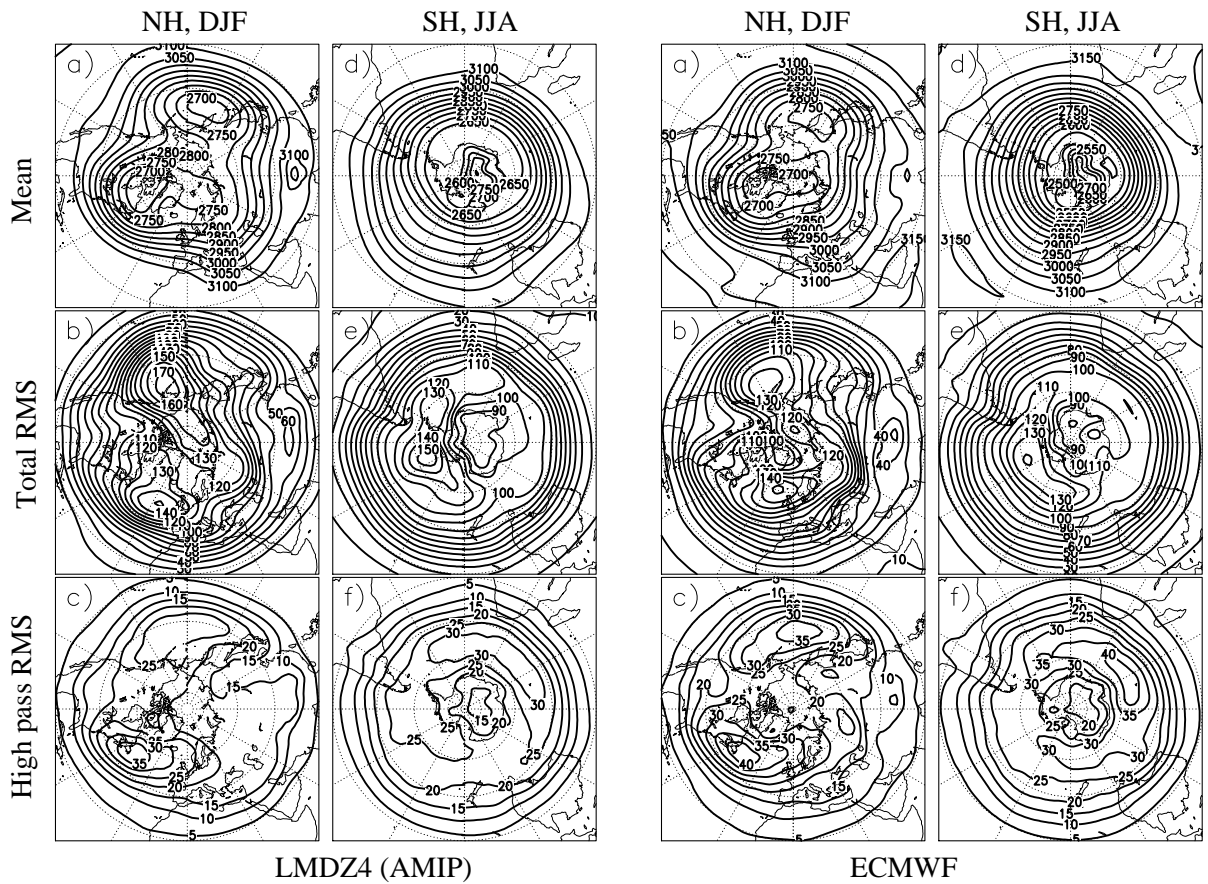


Figure 3: Winter statistics of 700hPa geopotential height for 20 winters and from the LMDZ4 model (left side) and ERA40 ECMWF analysis (right side) for the Northern Hemisphere in December-January-February (NH, DJF) and for the Southern Hemisphere in June-July-August (SH, JJA). (a)-(d) winter mean contour, interval 50m; (b)-(e) RMS, contour interval 10m; (c)-(f) RMS high pass, contour interval 5m

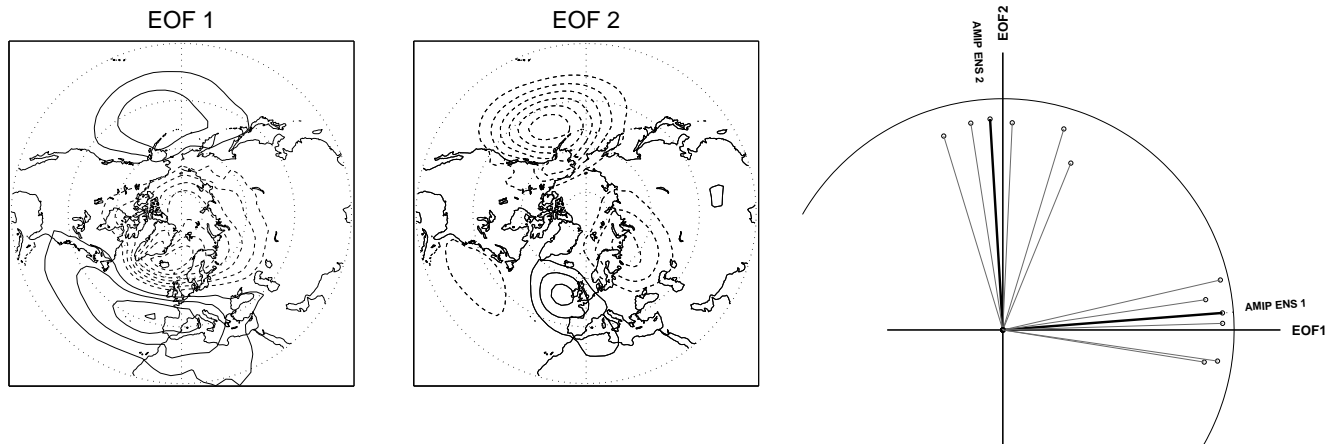


Figure 4: Leading 2 EOF of monthly wintertime northern hemisphere SLP, 1980-2001 (Contours every 1hPa) and projections (area-weighted correlations) of the EOF of the different simulations on the phase space defined by the two EOFs. For reference, a circle of radius unity is plotted. Thin lines are individual simulations, the thick lines are for the ensemble.

analysis of the ERA SLP for the 1980-2001 period are shown on Fig. 4. EOF1 is a quasi-zonally symmetric dipole between the polar and mid-latitudes also called the Northern Annular Mode or Arctic Oscillation (Thompson and Wallace, 1998). EOF2 on the other hand is a wavy pattern with a large center of action over the Pacific and a weaker secondary wave train over Europe. The two EOFs are orthogonal by construction.

Following Quadrelli and Wallace (2004), the first 2 EOF of each simulation are projected on the two basis patterns. The results are shown on figure Fig. 4: each EOF is represented by a line whose projections on the horizontal and vertical axes give the correlation with the basis EOF 1 and 2, respectively.

The lines gather around the two axes with a spread indicative of the variability between different simulations. An ensemble EOF, computed from all experiments together, is also shown. The simulated patterns of variability correlate very well with the observed basis functions, particularly for EOF1 which is the larger scale pattern.

3.5 High latitudes

The extreme polar climate is often rather poorly represented in global climate models (Chen et al., 1995), although it influences the global climate significantly and has a decisive impact on global sea level. To improve the representation of the polar near-surface climate, modifications of the boundary layer scheme have been implemented in LMDZ4 following Krinner et al. (1997). Over the ice sheets in particular, but also on the Arctic sea ice, data are scarce and the quality of gridded datasets often remains questionable. Therefore, in this section, model output is compared to station measurements over the relatively uniform plateau regions in the center of the ice sheets. Fig. 5 shows the simulated (altitude-corrected) and AWS-observed (Automatic Weather Stations Project, 2004; Automatic Weather Stations Greenland Project, 2004) monthly mean surface air temperatures at Summit (Central Greenland) and Dome C (Central East Antarctica).

Both sites are representative of the central plateau parts of the respective ice sheets. Apart from a slight cool bias at Summit, the model reproduces rather correctly the observations. This cool bias is probably caused by an underestimate of the downwelling longwave radiation, a relatively frequent model bias over ice sheets (e.g., King and Connolley, 1997). In Antarctica, this bias seems to be compensated for by a problem caused by a misrepresentation of orographic surface drag over the ice sheet slopes.

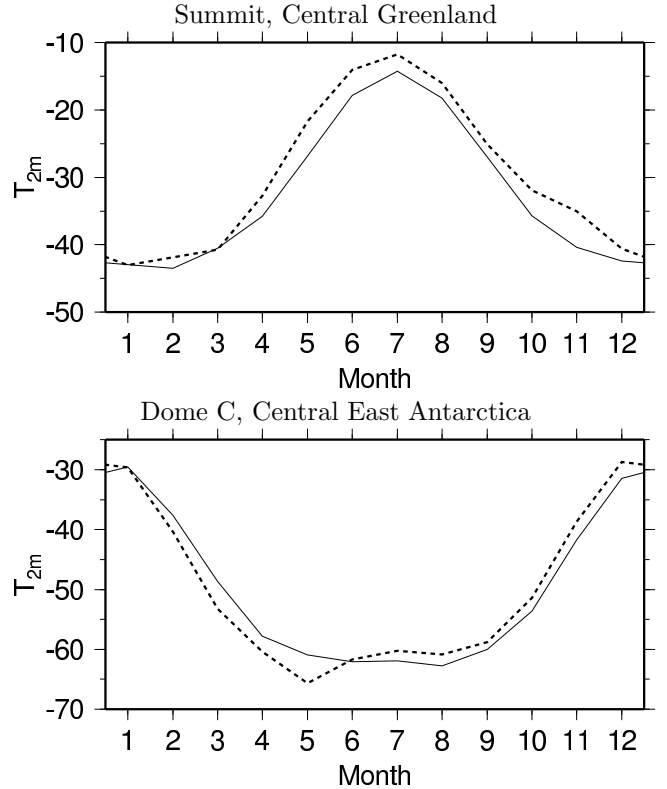


Figure 5: Monthly mean surface air temperatures at Summit (38°W , 72°N , 3250 m asl) and Dome C (123°E , 75°S , 3300 m asl) as simulated with LMDZ4 (full curve, AMIP simulation) and observed (dashed).

As noted by Krinner et al. (1997), the orographic roughness calculated from the subgrid variability of surface altitude is often too high over the ice sheet escarpment regions. This leads unrealistically to high surface drag over the ice sheet escarpments, which are in reality smooth sloping surfaces, and thus to an underestimate of the simulated surface wind speed over the continent margins, especially in winter, and thus a general underestimate of the intensity of the Antarctic katabatic drainage flow (James, 1989). Another consequence of this strong surface drag is probably a compensation of the underestimate of downwelling longwave radiation by downward sensible heat flux over large parts of Antarctica. Sensitivity tests with strongly decreased orographic roughness have shown strongly increased, and more realistic, surface wind speeds in Antarctica and a strong cooling (about 5°C) over the continent.

Precipitation over the polar regions (not shown) seems to be fairly correctly represented in the model. As direct precipitation measurements are essentially unavailable over the ice sheets because of

obvious problems in measuring the extremely low solid precipitation rates, the simulated surface mass balance over the central ice sheet regions is used as a surrogate here. In these areas, blowing snow is rare and melt does not occur because of the low temperatures. Therefore, the surface mass balance, which is easy to measure through shallow firn cores, is simply the difference between precipitation and evaporation/sublimation. Surface mass balance at Dome C (Antarctica) is 25 kg m^{-2} per year (community members, 2004); at Summit, it is approximately 220 kg m^{-2} per year (Shuman et al., 1995). The corresponding values for LMDZ4 are 43 kg m^{-2} per year for Dome C and 146 kg m^{-2} per year for Summit. Given the relatively low horizontal resolution of the model simulation, these values are acceptable. Over Antarctica as a whole, surface melt is weak; therefore, surface mass balance and precipitation minus evaporation can be roughly compared. The average simulated precipitation minus evaporation for Antarctica is 184 kg m^{-2} per year, which is not far from the current best estimate of surface mass balance of 166 kg m^{-2} per year (Vaughan et al., 1999). For Greenland, a similar ice-sheet wide assessment is not useful as, because of the low model resolution, the ablation zone is not properly captured by the model and because surface melt is a significant term in the surface mass balance of the ice sheet. Over the Arctic basin, available gridded precipitation maps (Arctic Climatology Project, 2000) indicate a wet bias (about 25 to 50%) of the model; however, as stated before, precipitation measurements in regions such as the Arctic basin are problematic because of the remoteness and the low precipitation rates.

4 Sensitivity to parametrized physics

In order to document the main developments and adjustments made to improve the climatology of the LMDZ model, we analyse here a series of sensitivity experiments focusing on the mean meridional structure and tropical divergent circulation and convection in the tropics.

4.1 Sensitivity experiments

The sensitivity experiments are conducted by using the averaged seasonal cycle of the AMIP boundary conditions and replacing one element or parameter of the reference version with an older version. The simulations are performed over 7 years, the last 6 of which are retained for analysis. The following

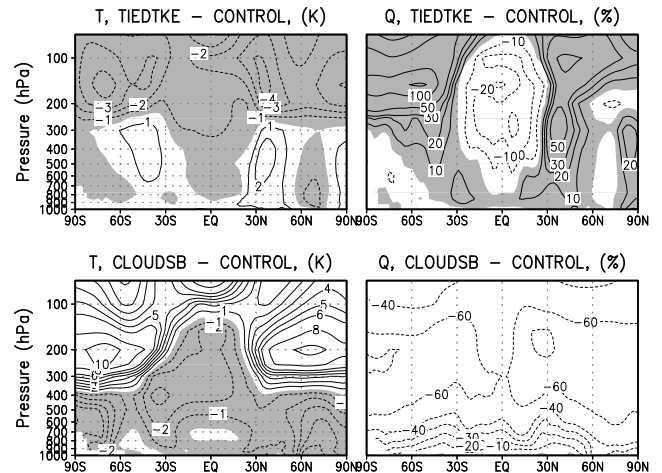


Figure 6: Impact of the convection (TIEDTKE, top) and cloud scheme (CLOUDSB, bottom) on the January mean temperature (left, difference between the sensitivity run and CONTROL) and humidity (right, relative difference between the sensitivity run and CONTROL in %). We use log pressure on the vertical in order to focus on the tropopause level. The shaded area correspond to a colder (left) and wetter (right) atmosphere in the sensitivity experiment.

simulations are considered here:

1. CONTROL: Same as AMIP simulations but with climatological SSTs. Used as a control for the sensitivity experiments.
2. TIEDTKE: The convection scheme is switched from Emanuel’s to Tiedtke’s. The radiative impact of convective clouds is also treated differently as explained above.
3. CLOUDSA: Coupling between the parametrized convection and cloud scheme (Bony and Emanuel, 2001) is not activated.
4. CLOUDSB: Same as CLOUDSA but with a wider PDF for subrid-scale water ($r_{\text{top}} = 1$ instead of 0.33).
5. BUCKET: The bucket scheme is activated in place of ORCHIDEE for the surface hydrology.
6. HIGHRES: Higher horizontal resolution with twice as many points as in the CONTROL in both longitude and latitude ($192 \times 145 \times 19$).

4.2 Mean meridional structure

Cold bias

In LMDZ, the magnitude of the tropospheric cold bias is quite sensitive to both the convection and cloud scheme. This is illustrated in Fig. 6 for the sensitivity experiments TIEDTKE and CLOUDSB (for January). The cold bias is about twice as strong in the TIEDTKE simulation as in the CONTROL (typically -8 K instead of -4 K) in the summer (southern) hemisphere. On the contrary, the CLOUDSB simulation is globally much warmer in the cold bias area; it even presents a significantly warm bias in the upper atmosphere, compensated by a cold bias in the lower troposphere. In both cases, the difference in the thermal structure originates from a modification in the atmospheric humidity content.

In the region of the cold bias, in the southern mid-latitudes, the air is up to twice as moist in TIEDTKE as in the CONTROL simulation (upper right panel of Fig. 6). The additional humidity comes directly from detrainment by the parametrization of cumulus convection. In fact, the Tiedtke and Emanuel schemes both predict a convective heating peaking well below 300 hPa in southern mid and high latitudes. But the Tiedtke scheme predicts an additional so-called "mid-level" convection with detrainment in the 250-100 hPa pressure range. This small but systematic import of water by detrainment is responsible for the additional humidity there, and for an increased radiation to space in the TIEDTKE simulation.

CLOUDSB experiment displays the opposite behavior. When using a wider distribution for the sub-grid scale water content, clouds are formed well before reaching saturation at large scale. Since part of the condensed water is eliminated by precipitation, the relative humidity is also much weaker. Therefore, the atmosphere is much drier than in the CONTROL simulation and radiative cooling is weaker (and the atmosphere much warmer) in the optically thin upper troposphere. Consistently, because of the weaker atmospheric extinction, the longwave radiation escapes more easily from the lower troposphere resulting in a colder atmosphere there.

Temperature differences as large as those shown in Fig. 6 do not contribute to significantly modify the latitude of the jets. The shift in the jets is, in fact, due to the relatively coarse horizontal resolution (see the discussion of zonal wind stresses below).

We also show in Fig. 7 how the different improvements or tunings affect the zonal mean rainfall (compared to the CMAP climatology Xie and Arkin, 1997), cloud radiative forcing and net absorbed radiation,

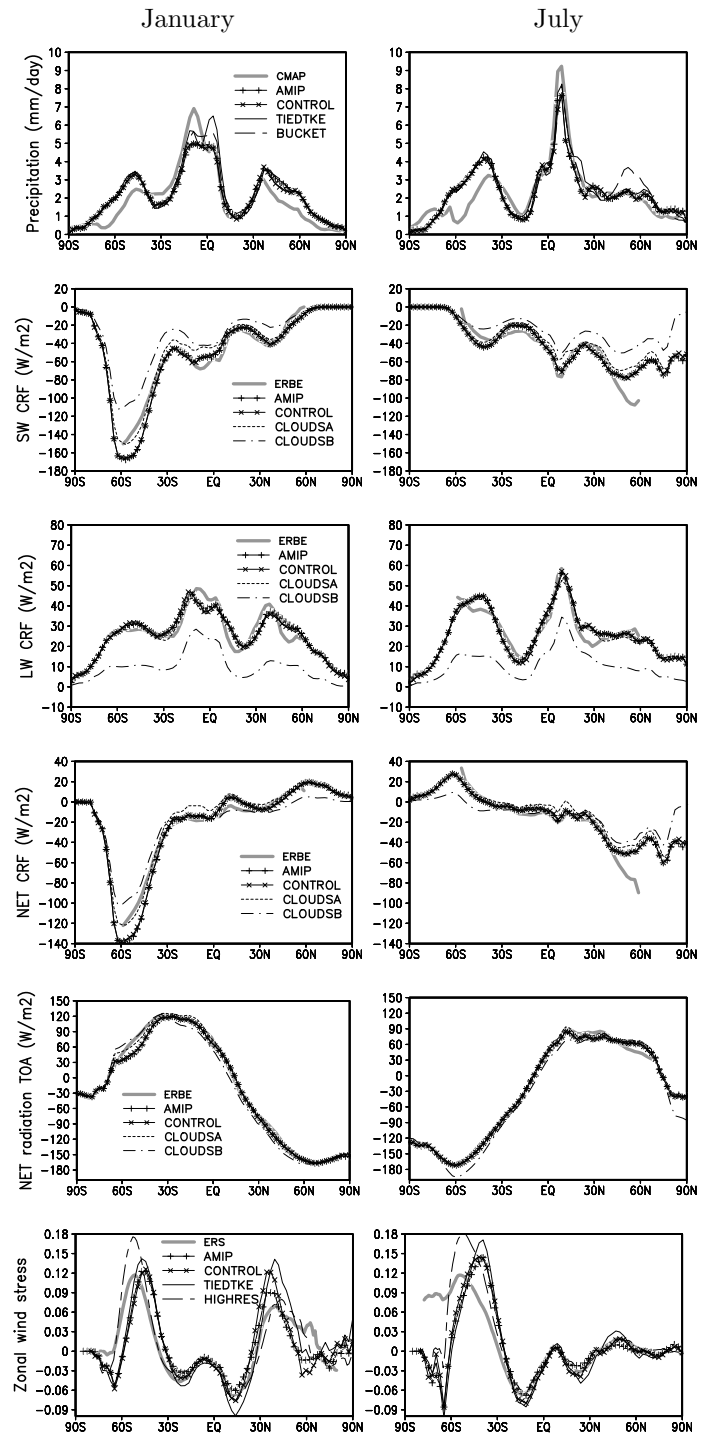


Figure 7: Zonally averaged rainfall (mm day^{-1}); shortwave (SW), longwave (LW) and net (NET) cloud radiative forcing (CRF , W m^{-2}); net absorbed radiation (W m^{-2}); and wind stress over the ocean (N m^{-2}). AMIP, control and a subset of the sensitivity experiments are compared to CMAP, ERBE and ERS observations.

ation (compared to ERBE data Barkstrom, 1984), as well as surface wind stress over oceans (compared to ERS scatterometer data). Superimposed to observations (grey), we show the AMIP results (+), the CONTROL simulation (\times , often superimposed) and results of the sensitivity experiments (thin curves). For clarity, each graph only considers a relevant subset of those experiments.

Rainfall

The mean rainfall is reasonably well represented in the AMIP and CONTROL simulations. The major biases concern the southern mid to high latitudes where the rainfall is overestimated for all seasons, and an underestimation of the rainfall in the southern tropical band in January. The introduction of the Orchidee scheme in place of the old bucket scheme for soil moisture results in a better representation of summer rainfall in the mid latitudes over continents. This summer rainfall is strongly overestimated with the bucket scheme as visible in July in the 40-70°N latitude band. Note also, for January, an underestimation of the rainfall at 10°S, corresponding to an underestimation of the SPCZ. In the TIEDTKE simulation, the rainfall is even slightly stronger at 10°N than at 10°S.

Clouds

As stated above, particular care was given to the tuning of the cloud radiative forcing, and in particular to the latitudinal variations of it. The overall agreement with ERBE observations is good, especially in the tropics. The CLOUDSA simulation has a weaker (less negative and farther from ERBE observation) shortwave radiative forcing in the tropics. Beyond physical consistency, this is the main reason why the Bony and Emmanuel (2001) approach was adopted. The CLOUDSB simulation shows a very good representation of net cloud radiative forcing in the tropics, but this is due to a compensation between forcings that are too weak in both the longwave and shortwave radiation. As the CLOUDSB simulation is also much drier (see the discussion above), the total radiation absorbed by the Earth system is underestimated for this case (the clear sky longwave radiation to space being too strong).

Wind stress

The surface stress is a very important quantity for the coupling with oceans. The zonally averaged zonal stress over tropical oceans associated mainly to trade winds is well simulated for the AMIP and CONTROL

simulations. The intensity is a little bit overestimated with TIEDTKE (25°N). The latitudinal shift of the mid-latitude jets is clearly visible on those curves as well as the strong positive impact of an increase of the horizontal resolution (HIGHRES) in that respect. Note also that it is one of the rare diagnostics for which there is a significant difference between AMIP and CONTROL simulation.

5 Sensitivity to parametrized physics

5.1 Hadley-Walker circulation

Annual mean

In order to characterize the tropical divergent circulation in the tropics in the various sensitivity experiments, we first consider the scalar potential φ_{200} of the horizontal wind at 200 hPa. The scalar potential is defined from the decomposition of the horizontal velocity \vec{V} into its divergent and rotational parts as

$$\vec{V} = \vec{\nabla}\varphi + \vec{\nabla} \wedge \vec{\psi} \quad (3)$$

The Laplacian of the scalar potential φ is also the wind divergence

$$\vec{\nabla} \cdot \vec{V} = \nabla^2 \varphi \quad (4)$$

A local minimum of the velocity potential at 200 hPa corresponds to a horizontal divergence and is generally associated to a large scale ascendance in the atmospheric column. This pressure level is generally retained for analysis because the divergence is generally maximum there. This is true on average, but a divergence below 200 hPa can be missed in the velocity potential even for a strong ascendance but confined to lower pressures. In order to analyse this problem, we shall also present a more synthetic view provided by the velocity potential $\tilde{\varphi}$ associated to the vertically integrated horizontal transport of geopotential $\int_0^{P_s} dp \vec{V} g z$. This potential is close to a z -weighed average of the velocity potential

$$\tilde{\varphi} \simeq \int_0^{P_s} dp z \varphi \quad (5)$$

It is shown in Appendix B that

$$\tilde{w} \simeq -\frac{1}{g} \nabla^2 \tilde{\varphi} \quad (6)$$

where \tilde{w} is the total vertical momentum of the atmospheric column

$$\tilde{w} = \int_0^\infty dz \rho w = - \int_0^\infty dz \frac{\omega}{g} \quad (7)$$

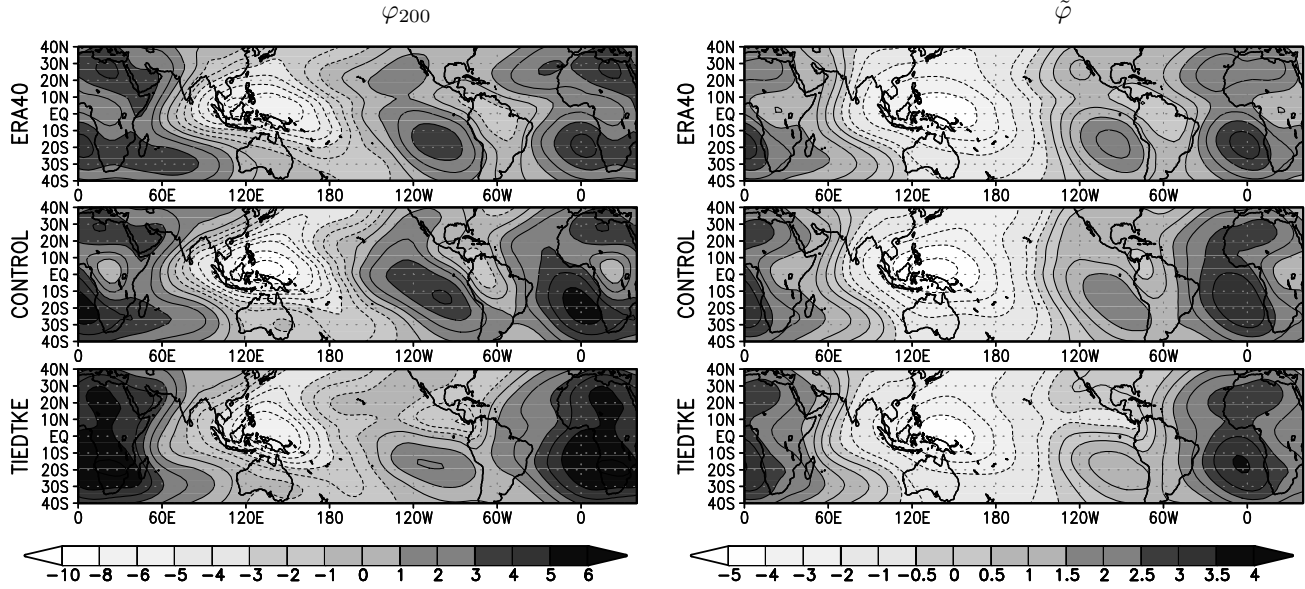


Figure 8: Scalar potential of the wind at 200 hPa (φ_{200} , left, unit $10^6 \text{ m}^2 \text{ s}^{-1}$) and of the geopotential transport ($\bar{\varphi}$, right, unit 10^{15} W); annual mean for the 1980-2002 period for ERA40 and for a 6-year average for CONTROL and TIEDTKE simulations.

The **scalar potential** φ_{200} of the 200 hPa annual mean horizontal wind is displayed in the left panels of Fig. 8. In the reanalysis, the overall structure of φ_{200} is characterized by a strong minimum (maximum ascending motion or large scale convection) over the western equatorial Pacific. Secondary minima, associated with the tropical forests over Africa and Amazonia are also visible as well as the maxima associated to dry subsiding regions on the eastern side of the tropical Atlantic and Pacific oceans.

This structure is reproduced reasonably well in the CONTROL simulation. Among the main differences, one can note that the trough of the equatorial East Pacific is not as marked as in the reanalysis. The minimum over Amazonia is also somewhat more confined and shifted toward central America than in the reanalysis. More quantitatively, one may notice that the potential variation between the West and East equatorial Pacific is about 30% larger in the CONTROL simulation.

In comparison, the TIEDTKE simulation shows significant differences, the most noticeable being the quasi disappearance of the potential minimum over Africa and the shift of the Amazonia minimum towards the equatorial East Pacific.

The **scalar potential** $\bar{\varphi}$ of the annual mean geopotential transport is displayed in the right panels of Fig. 8. As expected, the weighted potential $\bar{\varphi}$ maps are quite similar to the velocity potential φ_{200}

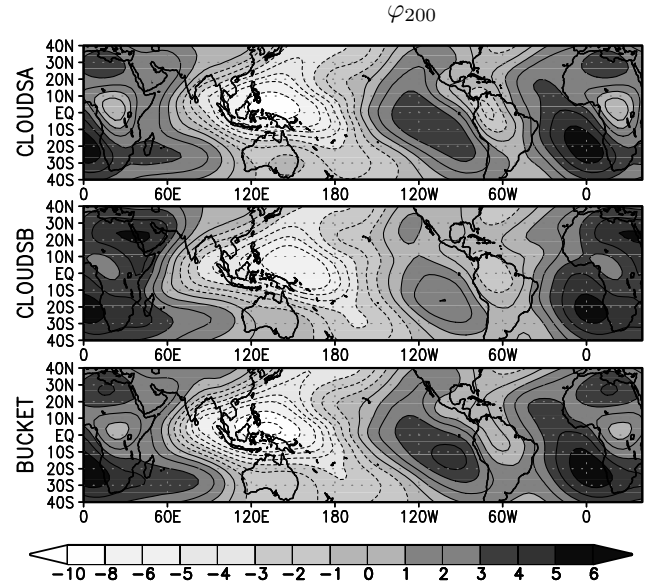


Figure 9: Scalar potential of the wind at 200 hPa (φ_{200} , unit $10^6 \text{ m}^2 \text{ s}^{-1}$); annual mean for a 6-year average for CLOUDSA, CLOUDSB and BUCKET sensitivity experiments.

ones, the main difference being a clearer structure in meridional bands. In the CONTROL simulation, most of the comments made from the velocity potential φ_{200} remain true, except for the total variation of $\tilde{\varphi}$ over the equatorial Pacific which is quite close in CONTROL and ERA40. The situation is more contrasted for the TIEDTKE simulation: the $\tilde{\varphi}$ field is closer to ERA40 over continents (some potential trough is present over East Africa while absent in φ_{200} field) and displays greater differences over ocean (a strong trough is associated to the ITCZ over the eastern equatorial Pacific).

The two potentials $\tilde{\varphi}$ and φ_{200} considered together yield indications about the vertical distribution of vertical velocity, which is, for a large part, related to the vertical distribution of convective heating. The fact that the CONTROL and ERA40 $\tilde{\varphi}$ fields agree better than the corresponding φ_{200} fields suggest similar structures for the total convective heating together with different vertical distributions. The large scale divergence associated to continental convection peaks higher in the simulation than in the re-analysis. The same comparison of $\tilde{\varphi}$ and φ_{200} for the TIEDTKE simulation suggests a relatively lower height for the large scale divergence over Amazonia and Africa than in the re-analysis.

For the CLOUDSA experiment, the φ_{200} minima over Africa and Amazonia are deeper than in the CONTROL (Fig. 9). It is the opposite for CLOUDSB which tends to mimic the relative weakness of continental convection in TIEDTKE. The $\tilde{\varphi}$ fields are in fact very close to each other over Africa and Amazonia for the CLOUDSB (not shown) and TIEDTKE simulations. However, the associated minima in φ_{200} still appear for CLOUDSB while they are absent for TIEDTKE. This suggests again that the use of Tiedtke’s scheme in place of Emanuel’s does not affect only the strength of the continental convection but also the vertical distribution of convective heating.

Finally, the BUCKET simulation is not very different from CONTROL with possibly a better representation of the large scale convection over Amazonia but a worse representation of the African trough which is shifted to the east.

Seasonality and rainfall

The changes analysed above in terms of large scale annual mean circulation have significant signature in terms of seasonal rainfall.

Differences of precipitation maps are usually difficult to interpret because they are often dominated by small shifts in the spatial structure. However, changes

in precipitation maps can be interpreted by comparison with differences in the large scale circulation.

For January, three of the sensitivity runs (TIEDTKE, CLOUDSB and BUCKET) show a similar pattern on the western side of the Indian ocean, with a large and unrealistic maximum of precipitation north-east of Madagascar (Fig. 10, left). This is a classical bias of a number of global models. This feature is related to a weakening of the large scale convection over the south of Africa and Amazonia (positive difference Fig. 10, right). Across the Indian Ocean, the Walker circulation is also reinforced with a weaker ascent in the Indonesian sector.

For July, a similar weakening of continental convection in TIEDTKE simulation is associated with a longitudinal structure of wave number 1 (Fig. 11). The large scale convection is globally weakened in the 0-160E longitude band, and monsoon rainfall are less abundant over the Indian and African continents. For India, this can be considered as an improvement with respect to CONTROL simulation which produces too much rain over the continent and not enough on the west coast.

In both January and July, the Tiedtke’s scheme also tends to produce narrow and strong rainfall longitudinal bands. This is the case for instance on the West Pacific north of the equator in January and south of the equator in July as well as over Africa during the rainy season (Fig. 10 and Fig. 11). This default is visible all year round north of the Equator in the East Pacific and corresponds to the strong trough in the annual mean velocity potential (Fig. 8).

5.2 Regime sorted analyses

In order to interpret the results just shown, we analyse the effect of the parametrization of diabatic processes at a given large scale dynamical regime, using as a proxy the vertical velocity at 500 hPa, ω_{500} , as proposed by Bony et al. (2004). Following previous studies, we keep ω_{500} as a proxy although $\nabla^2\tilde{\varphi}$ is a promising alternative (see Appendix B). The regime sorting is done on a monthly basis and for the 30°S-30°N region.

When comparing two different parametrizations in this framework, one must keep in mind the underlying probability distribution function giving the relative weight of the various regimes. Fig. 12 shows the PDF obtained from the most recent reanalysis datasets and from various simulations. It is interesting to note that the PDF is sensitive to the parametrization. One can notice for instance the profound modification of the PDF in subsiding regimes ($\omega_{500} > 0$) for the CLOUDSB case and the bump in the distribution in convective

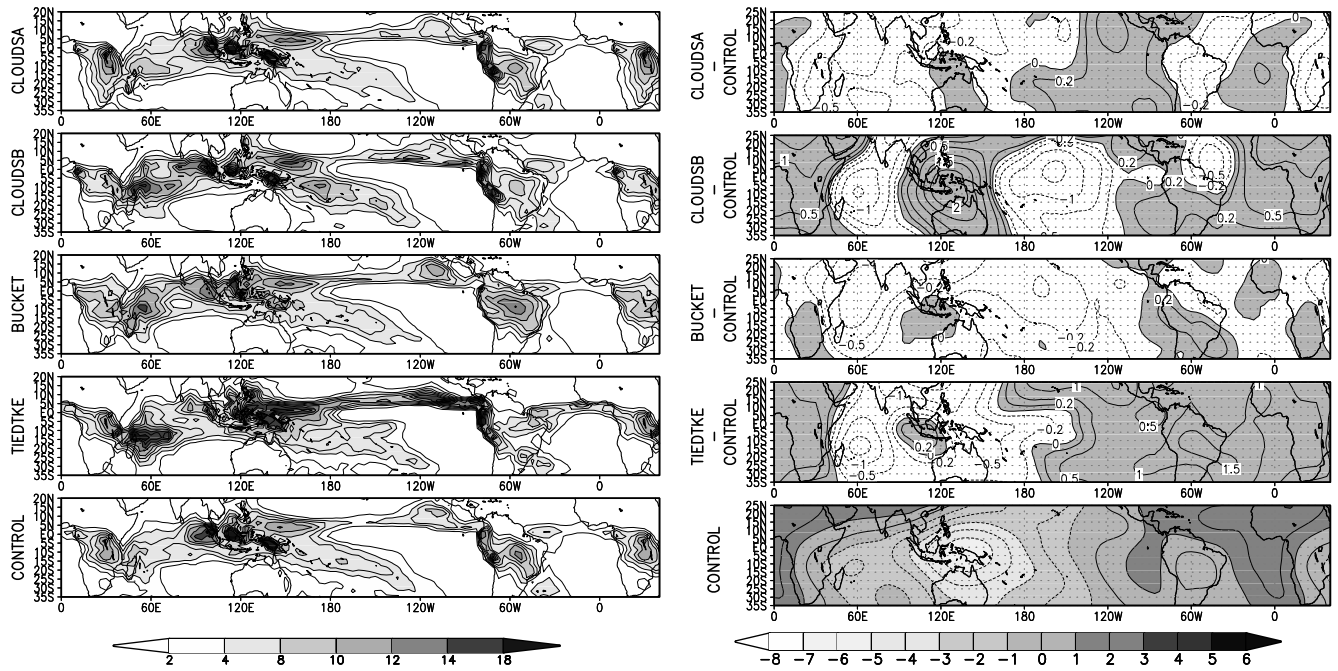


Figure 10: January rainfall (left, mm d⁻¹) and potential $\tilde{\varphi}$ (right, unit 10¹⁵ W) for the CONTROL and sensitivity experiments. For the sensitivity experiments, the right panel is the difference of $\tilde{\varphi}$ with that of the CONTROL simulation with same units.

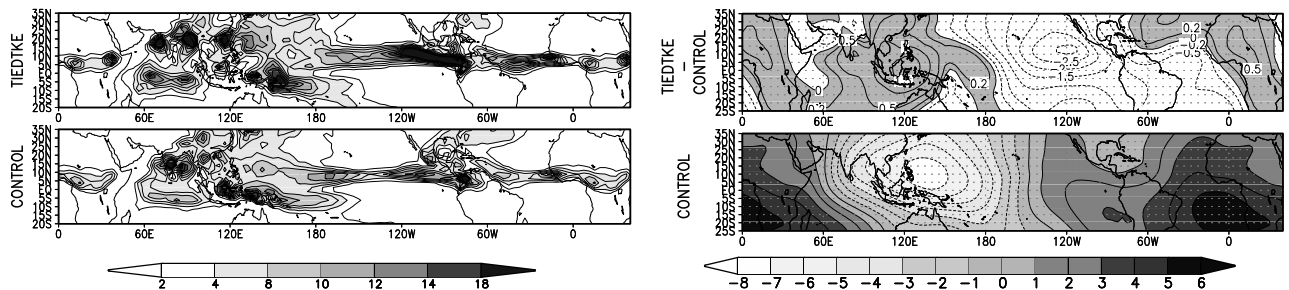


Figure 11: Same as Fig. 10 but for July and CONTROL and TIEDTKE.

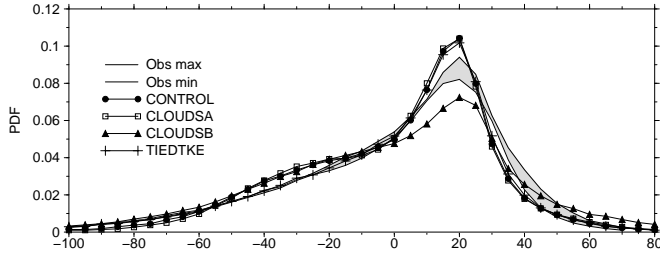


Figure 12: Probability distribution function of ω_{500} in the 30S-30N latitude band over oceans for two set of reanalysis (ERA40 and NCEP2 giving rise to the gray area) and for the CONTROL, CLOUDSA/B and TIEDTKE experiments.

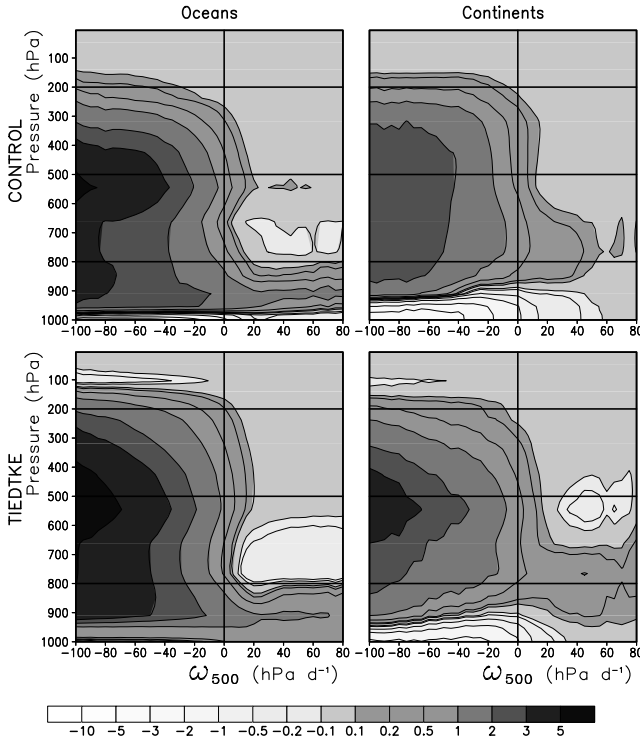


Figure 13: Convective heating rate (K d^{-1}) in a regime sorted diagram (pressure in hPa versus ω_{500} in hPa d^{-1}) for the CONTROL (with Emanuel's scheme) and TIEDTKE experiments over oceans (left) and continents (right).

regimes for the CONTROL and CLOUDSA/B cases, between -20 and -50 hPa d^{-1} , which is neither present in the reanalysis nor in the TIEDTKE simulations.

Convection scheme

In order to compare the convective parametrizations (CONTROL simulation with Emanuel's scheme and

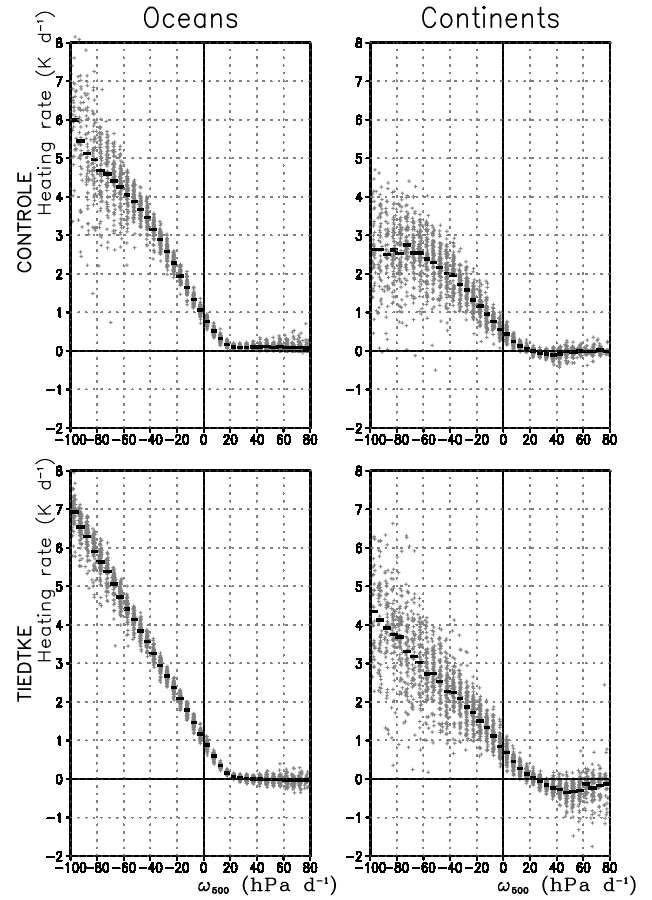


Figure 14: Scatter plot of the convective heating rate (K d^{-1}) at the 550 hPa pressure level, as a function of ω_{500} (hPa d^{-1}).

TIEDTKE with Tiedtke's scheme) in the regime sorted framework, we shall use a series of figures displaying annual means of various quantities averaged over the 30S-30N latitude band (convective heating rate, convective moistening, relative humidity and cloud cover) in ω_{500} -pressure graphs.

First we consider the general features of these graphs. Fig. 13 displays the convective heating rate ω_{500} -pressure graphs. The distinction between deep convection for ascending regimes ($\omega_{500} < 0$) and shallow convection for subsiding regimes ($\omega_{500} > 0$) is the first thing to notice on all the graphs. The difference between continents and oceans is also well marked with a cooling by convection in a very shallow layer close to the surface over the ocean and in a much thicker layer over land. The heating rate by convection increases less rapidly as a function of $-\omega_{500}$ over continents because there is less water available there. This contrasted behavior is further illustrated by a scatter plot (Fig. 14)

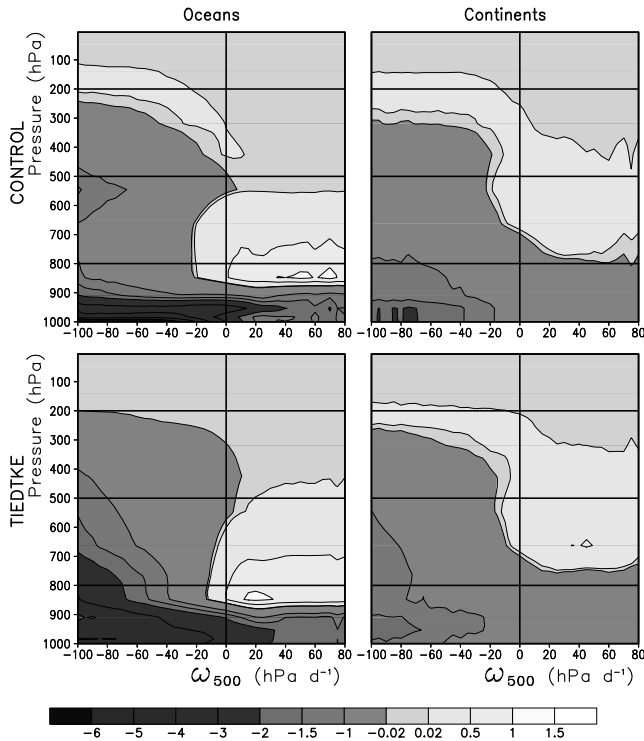


Figure 15: Convective moistening ($\text{g kg}^{-1} \text{d}^{-1}$) with same conventions as in Fig. 13.

showing the same heating rates as in Fig. 13 but for the 550 hPa pressure level. Each point on these graphs corresponds to one point of the horizontal grid and one of the 6×12 months of the simulation used to produce the regime sorted analyses. Note the relatively weak dispersion around the mean.

The associated moistening (Fig. 15) is also well characterised. In deep convective regimes ($\omega_{500} < 0$), the parametrization essentially dries the whole atmosphere by precipitating water onto the ground. For shallow convection ($\omega_{500} > 0$), the water is transported from the surface up to the 850-500 hPa pressure range over oceans (with a similar but weaker effect on continents). Near the surface, the (dominant) effect of downdraughts results from the combination of moistening (and cooling) by evaporation of precipitation from above and drying (and heating) by downward advection. On continents, because of the relatively weak relative humidity (see Fig. 16), a large part of the precipitation evaporates in the boundary layer, explaining the weak drying and strong cooling there. It is just the opposite over ocean. The near saturated boundary layer inhibits evaporation and the strong stratification in humidity leads to stronger positive drying and heating by downward advection.

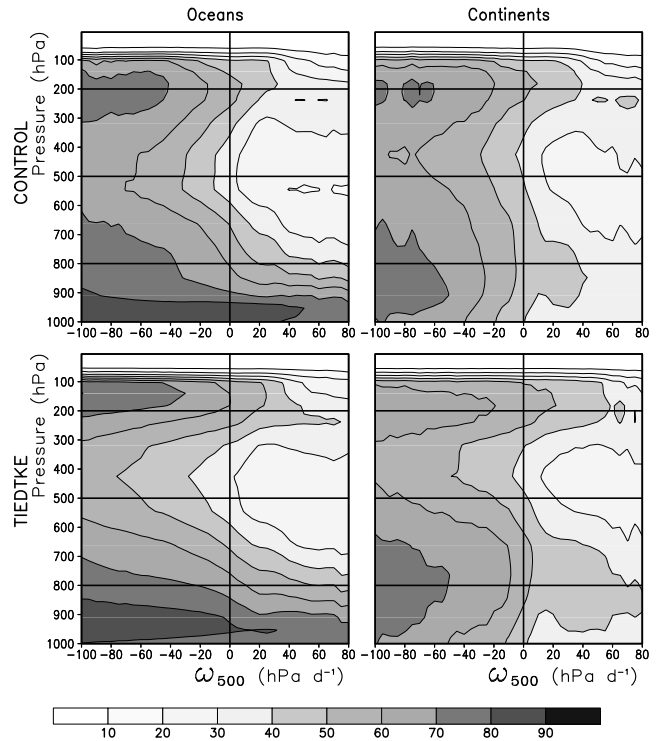


Figure 16: Relative humidity (%) with same conventions as in Fig. 13.

Turning to the the comparison of the two convective schemes, the vertical distribution of convective heating (Fig. 13) appears quite different. Tiedtke's scheme produces a deeper convection over oceans than Emanuel's. The vertical distribution is also different on continents. The heating rate peaks at 550 hPa with Tiedtke's scheme (like over the ocean). The convective heating is more homogeneous on the vertical with Emanuel's, corresponding to a stronger heating above 500 hPa. The convection is finally significantly stronger and higher over ocean than over continent with Tiedtke's. With Emanuel's, the convection is somewhat deeper and only slightly weaker on continents. This differences are consistent with the differences in the velocity potential discussed above, with a weaker and shallower large scale convection over continents when using Tiedtke's scheme.

Note also that the dispersion of heating rates around the mean (Fig. 14) is somewhat larger over oceans for Emanuel's scheme, which can be understood since the closure in moisture convergence used in Tiedtke's scheme does not leave many degrees of freedom for the parametrization over the ocean, where humidity is close to saturation, and the convergence of mass is strongly correlated to the variable used as an abscissa for the

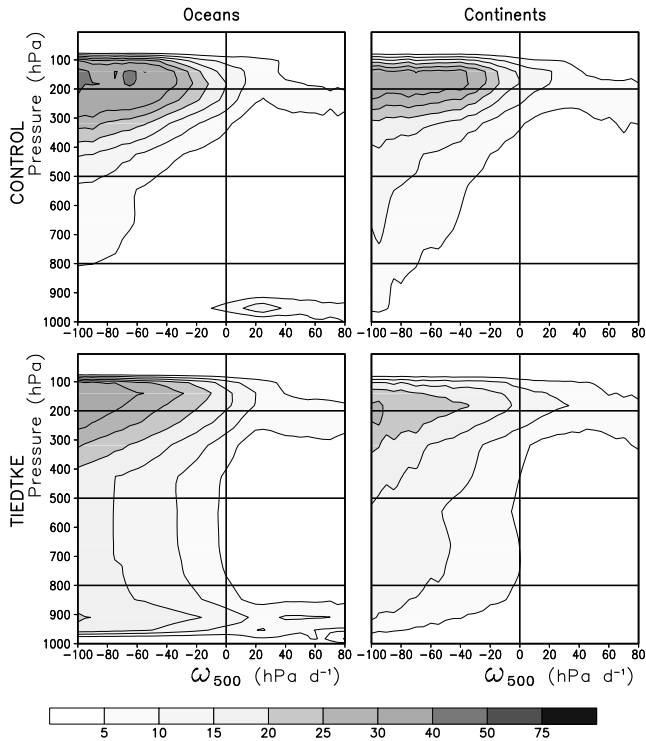


Figure 17: Cloud cover (%) with same conventions as in Fig. 13.

plot. Since the convective intensity is proportional to ω_{500} , it is not bounded. Tiedtke’s scheme can thus lead to positive feedback loops of CISK nature (which may be related to the “grid-point storms” observed in old versions of the ECMWF model). For Emanuel’s scheme, the convective intensity seems to saturate for strong vertical velocities, which is more conform to observations of precipitation (not shown). For intermediate regimes ($-50 \text{ hPa d}^{-1} < \omega_{500} < 0$) however, both parametrizations show a remarkably weak dispersion, consistently with the picture of a quasi-equilibrium between convection and large scale dynamics in the tropics.

One can notice other differences between the two convection schemes. There is a thin layer of cooling around 100 hPa in TIEDTKE simulation which has no counterpart in the CONTROL simulation. The CONTROL simulation shows a systematic moistening between 250 and 150 hPa which is predicted by TIEDTKE simulation on continents but not on oceans. The two parametrizations predict quite different heating rates in the subsiding regimes, especially over continents.

The associated cloud covers are shown in Fig. 17. The fractional cover of mid level clouds in convective

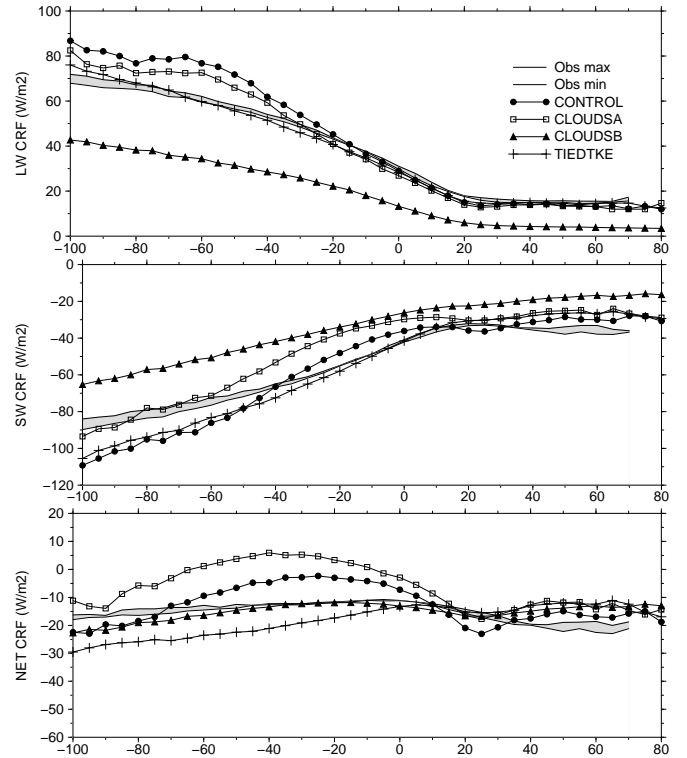


Figure 18: Cloud radiative forcing (CRF) in the 30S-30N latitude band over ocean (top: long wave CRF; middle: short wave CRF; bottom: net CRF)

regimes is much larger with Tiedtke’s scheme, since the cloud cover is imposed as a constant between cloud basis and top when convection is activated in a grid cell. By comparison, Emanuel’s scheme coupled to Bony and Emmanuel (2001) scheme for clouds produces less clouds below 500 hPa. In both simulations, there are very few boundary layer clouds in subsiding regimes over continents. Independent tests suggest that those clouds, and in particular boundary layer cumulus clouds, may be strongly underestimated by the model.

Cloud scheme

Most of the changes observed in the large scale organisation of convection for CLOUDSA and B (Fig. 9) can be explained by looking at cloud radiative forcing in the regime-sorted framework (Fig. 18).

First the CONTROL simulation shows reasonable agreement with ERBE observations. In subsiding regimes ($\omega_{500} > 0$), the three radiative longwave, shortwave and net radiative forcings are reasonably close to the observation on the average. For the intermediate regimes, the agreement is better for the longwave radiative forcing but results in a net negative forcing which is not strong enough. For strong

	CRFNET	CRFLW	CRFSW	LWTOP	NETTOP	SWS	T2M	PRECIP	EVAP
CONTROL	-5.3	51.5	-56.7	-237.0	70.9	225.1	25.6	5.3	4.2
Difference with CONTROL									
TIEDTKE	-13.4	-6.8	-6.7	-8.6	-14.8	-9.5	0.6	1.4	0.6
CLOUDSA	7.5	-4.4	11.9	-4.5	6.7	12	-0.1	0	0
CLOUDSB	-8.3	-26.6	18.2	-37.8	-20.8	17.5	-0.5	0.8	0.8
BUCKET	-1.4	-2.1	0.5	-1.8	-2.1	-0.4	-0.1	0.2	0.1

Table 1: Net (CRFNET, $W m^{-2}$), longwave (CRFLW, $W m^{-2}$) and shortwave (CRFSW, $W m^{-2}$) cloud radiative forcing, infrared radiation to space (LWTOP, $W m^{-2}$), net radiative budget at top of atmosphere (NETTOP, $W m^{-2}$), total solar radiation absorbed by the surface (SWS, $W m^{-2}$), air temperature at 2m above surface (T2M, Celcius), precipitation (PRECIP, $mm d^{-1}$) and evaporation (EVAP) averaged for convective regimes ($-100hPa d^{-1} < \omega_{500} < 0$) over oceans between 30S and 30N.

	CRFNET	CRFLW	CRFSW	LWTOP	NETTOP	SWS	T2M	PRECIP	EVAP
CONTROL	1.6	47.9	-46.3	-241.5	54.0	212.9	24.5	3.9	1.9
Difference with CONTROL									
TIEDTKE	-15.7	-12.3	-3.4	-12.1	-16.5	-6.4	-0.1	-0.5	-0.1
CLOUDSA	7.9	1	6.9	0.8	5.9	6	0.1	0.3	0.1
CLOUDSB	-8.4	-26.2	17.8	-35.3	-22.5	17.1	-1.6	-0.3	0
BUCKET	-13.5	-2.3	-11.2	0	-9	-9.3	-2	0.7	1.3

Table 2: Same as Table 1 but for continents.

convective regimes, between -90 and $-60 hPa d^{-1}$, the cloud radiative forcing is overestimated but the net forcing is good because of a compensation of errors. It is worth mentioning that these regime-sorted data were not used at the time of the tuning of the model. The discrepancies between observations and simulation results are true measures of the defaults of the model.

The CLOUDSA experiment is very close to CONTROL in subsiding regimes (as expected). In convective regimes, activation of Bony and Emmanuel (2001) clouds scheme (CONTROL versus CLOUDSA) reinforces the (negative) shortwave radiative forcing by about $10-15 W m^{-2}$, with almost no effect in the longwave. Because of the smaller shortwave radiative forcing in CLOUDSA (with respect to CONTROL) more solar radiation can reach the surface. The mean solar radiation at the surface (SWS) is increased by $12 W m^{-2}$ on the averaged over the tropical oceans for convective regimes (Table 1) and by $6 W m^{-2}$ over continents (Table 2). This increased solar radiation increases the convection over continents but has almost no effect over ocean explaining the main differences observed in the velocity potential fields (Fig. 8 and Fig. 9).

As already mentioned, CLOUDSB is an extreme sensitivity experiment in which the much drier and less cloudy atmosphere (with respect to CONTROL) leads to a much larger infrared cooling to space. This

increased cooling is only partly compensated by the weaker backscattering of solar radiation by clouds. Over ocean with fixed SSTs, the larger cooling to space destabilizes the atmosphere and increases convection. This increased convection results in colder near-surface temperature over the ocean of an average of $0.5 K$ despite the imposed SSTs (Table 1). For the same reason, the continents cool down explaining the reduced large scale convection observed in Fig. 9. The near surface temperature is, on average, $1.6 K$ colder than in the control run over continents (Table 2).

Note that TIEDTKE simulation also has a slightly different radiative forcing than the CONTROL simulation. As for the CLOUDSB case, the net radiative forcing is more negative than in the CONTROL in convective regimes. Thus, the smaller ocean/continents contrast in TIEDTKE simulation may come partly from this difference in cloud radiative forcing. The stronger emission of infrared radiation to space may also explain in part the larger heating rate by the parametrized convection over oceans (to a first approximation, at a given vertical velocity, and for a fixed temperature lapse rate, the convective heating rate balances the infrared cooling to space).

However, the difference in cloud radiative forcing does not explain the fact that convective heating reaches higher levels over continent with Emanuel's scheme and over ocean with Tiedtke's. Nor will it

explain the very different organisation of convection over the east side of the pacific bassin.

Surface scheme

We finally explain the weakening of large scale continental convection in the BUCKET experiment. The bucket model tends to evaporate much more easily convective rainfall over continental convective regions. The effect on temperature (cooling by more than 2 K, Table 2) is probably dominant and explains the reduction in continental large scale convection. This effect is particularly clear in january over the Indian ocean as explained below. In July (not shown) the rainfall over india is even better in the sense that it extends farther north-west, toward Pakistan. This improvement is probably due to a local coupling: the rapid cooling of the surface by faster evaporation of convective rainfall (with respect to the CONTROL simulation) favors a triggering of convection in the very hot regions further north. The impact over African monsoon is however very weak.

6 Concluding remarks

The developments and tuning of the new version of the IPSL coupled model has driven a number of development and tunings which altogether define the new cycle, LMDZ4, of the LMD atmospheric general circulation model. As usual, the tuning phase is the result of compromises. The model must represent correctly different regions of the globe, different climate regimes, means and variability at different scales, and so on. For coupling with other components, the model must also reproduce satisfactorily the radiative and turbulent fluxes at the surface as well as convective and turbulent transport for the coupling with chemistry and aerosols microphysics. The LMDZ4 model presents altogether a rather satisfactory climatology, even in the very high latitudes, a reasonable representation of the mid-latitude variability at synoptic and interannual scales as well as a reasonable latitudinal distribution of rainfall, radiative forcing and wind stresses. When coupled to the ORCALIM oceanic model, it also reproduces a rather satisfactory seasonal cycle and interannual variability in the tropics (Marti et al., 2005).

The model however still exhibits significant biases. First, the mean thermal structure exhibits a cold bias of several K in high latitudes in the 400-150 hPa pressure range. This bias is sensitive to the transport of water in that region, an increase in water reinforcing the infrared cooling to space there. It is possible that finer

tuning of the cloud scheme could produce a reduction of this bias. Note also that a peculiar behavior of the LMDZ version of Tiedtke scheme was identified there, with a moistening by convection well above the main convective layer in mid and high latitudes. This moistening reinforces in turn the cold bias. A second important bias is a systematic shift of the winter jets toward the equator, a bias which is mainly attributable to the rather coarse horizontal resolution retained for the climate change simulations. The model also tends to produce monsoon rainfalls that are spatially too confined. Part of the explanation could come from the coupling with the surface scheme as suggested by the better extension of the indian monsoon toward Pakistan with the BUCKET scheme (result not shown). Note also that a numerical problem in the surface scheme was identified after the realisation of the IPCC simulations. It produces occasionally very cold temperatures over one time-step in very dry continental regions in the tropics. The cloud radiative forcing still exhibits some biases as well. It could also probably be tuned further but the agreement is reasonable in view of the previous generation of climate models (Bony et al., 2004).

Despite those biases, the LMDZ4 version represents a significant step further with respect to the previous LMDZ3 version (see e. g. Li and Conil, 2003) which was used for a number of chemical applications (Boucher and Pham, 2002; Hauglustaine et al., 2004).

A major improvement arises from the improvement and tuning of the parametrization of convection and clouds. We have shown in particular that the replacement of the Tiedtke convection scheme by Emanuel's scheme has a major and generally positive impact in the tropics. The vertical distribution of convective heating is affected with a contrasted behavior on land and ocean. The convective heating is relatively higher over continents with Emanuel. As a consequence, the troughs of the velocity potential at 200 hPa over continents in the tropics are simulated better with the Emanuel's scheme. The Tiedtke's scheme also tends to produce marked patterns of concentrated rainfall over oceans, a feature most probably attributable to the CISK mechanism. The parametrization of clouds has also a significant impact on the relative intensity of large scale convection over land and ocean. The coupling of the convection scheme with clouds (CLOUDSA versus CONTROL experiment) according to Bony and Emmanuel (2001) has a positive impact by reinforcing the backscattering of solar radiation by convective clouds, thus cooling and reducing the convection over continents. This continental convection is probably still a little bit too strong in the standard version when compared to

ERA40 reanalysis.

Using on the one hand the velocity potential to characterize the large scale circulation and, on the other, regime-sorted diagnostics of the physical parametrizations, turns out to be useful framework to analyse the coupling between large scale dynamics and parametrized processes. The potential associated to the horizontal transport of geopotential is also particularly meaningful since it gives an integrated view of the large scale convection, directly related to the total vertical momentum of the atmospheric column.

The modifications of the large scale divergent circulation has very important implications for the coupling with the ocean. For instance, the erroneous maximum of precipitation observed on the Indian Ocean, north-east of Madagascar, in three of the sensitivity experiments (CLOUDSB, BUCKET and TIEDTKE) is associated with a strong underestimation of the eastward equatorial wind stress over the Indian Ocean (converging over Indonesia), or even with a stress in the wrong direction (toward the west).

As explained in the model description, the version with Tiedtke's scheme presented here is already a tuned version of the LMDZ3 model. The cloud radiative forcing obtained with it is as close to the observation as that of the standard version with Emanuel's convection scheme. Altogether, both the Emanuel and Tiedtke versions were tuned to less than 1 W m^{-2} on average for the global exchange with space. These two versions of the same model, which only differ in the treatment of the cumulus convection and associated clouds, have been used to further analyse the impact of the parametrized physics on the coupling with ocean and on the climate response to an increase of the concentration of greenhouse gases. The results of those simulations will be analysed in a companion paper.

Lastly, it should be noted that a number of key features of the model climatology were obtained with adhoc tunings of a rather obsolete version of the parametrization of boundary layer transport. In particular, different treatments are used on oceans, to simulate the contrasts between strato-cumulus and trade-winds cumulus, and on continents, where a minimum diffusivity is introduced to control the strength of the polar inversion. It has been identified since that this same threshold results in an unrealistic reduction of the diurnal cycle of trace constituents emitted at the surface on continents (result not shown). Independent work on the parametrization of the vertical transport in the boundary layer should soon lead to a new set of physical parametrization for the LMDZ model. In this new version, the thermal plume model of Hourdin et al. (2002) will be used to account

explicitly for the organized structure of the boundary layer, introducing an additional scale between the small scale turbulence of the surface boundary layer and the scale of the deep convection. Coupled to an improved version of the convection scheme (Grandpeix et al., 2005), and to the clouds scheme of Bony and Emmanuel (2001), we hope that this new scheme will help improve the representation of boundary layer clouds on oceans (crucial for climate sensitivity) as well as the representation of the diurnal cycle of cumulus convection, identified as a major bias of current general circulation models (Guichard et al., 2004).

References

- Arctic Climatology Project, Environmental working group arctic meteorology and climate atlas, cD-Rom, 2000.
- Automatic Weather Stations Greenland Project, Greenland aws data, digital data available on <http://amrc.ssec.wisc.edu/greenland.html>, 2004.
- Automatic Weather Stations Project, Archive aws data, digital data available on <http://amrc.ssec.wisc.edu/aws.html>, 2004.
- Ball, J., I. Woodrow, and J. Berry, 1987, A model predicting stomatal conductance and its contribution to the control of photosynthesis under different environmental conditions, *Progress in Photosynthesis*, 4, 221–224, 1987.
- Barkstrom, B. R., 1984, The earth radiation budget experiment (ERBE), *Bull. Am. Meteorol. Soc.*, 65, 1170–1185, 1984.
- Blackmon, M. L., 1976, A climatological study of the 500 mb geopotential height of the northern hemisphere, *J. Atmos. Sci.*, 33, 1607–1623, 1976.
- Bony, S., and K. A. Emmanuel, 2001, A parameterization of the cloudiness associated with cumulus convection; evaluation using TOGA COARE data, *J. Atmos. Sci.*, 58, 3158–3183, 2001.
- Bony, S., J.-L. Dufresne, H. Le Treut, J.-J. Morcrette, and C. Senior, 2004, On dynamic and thermodynamic components of cloud changes, *Climate Dynamics*, 22, 71–86, 2004.
- Boucher, O., and M. Pham, 2002, History of sulfate aerosol radiative forcings, *Geophys. Res. Lett.*, 29, (9), 2002.

- Braconnot, P., S. Joussaume, O. Marti, and N. Noblet, 1999, Synergistic feedbacks from ocean and vegetation on the african monsoon response to mid-Holocene insolation, *Geophys. Res. Lett.*, *26*(16), 2481–2484, 1999.
- Braconnot, P., Tests de sensibilité, Note technique 0076, IPSL, 1998.
- Chen, B., D. H. Bromwich, K. M. Hines, and X. Pan, 1995, Simulations of the 1979-1988 polar climates by global climate models, *Ann. Glaciol.*, *21*, 83–90, 1995.
- Collatz, G., M. Ribas-Carbo, and J. Berry, 1992, Coupled photosynthesis-stomatal conductance model for leaves of c_4 plants, *Aust. J. Plant Physiol.*, *19*, 519–538, 1992.
- community members, E., 2004, Eight glacial cycles from an Antarctic ice core, *Nature*, *429*, 623–628, 2004.
- Cosme, E., F. Hourdin, C. Genthon, and P. Martinerie, 2005, Origin of dimethylsulfide, non-sea-salt sulfate, and methanesulfonic acid in eastern Antarctica, *J. Geophys. Res.*, *110*, 3302+, 2005.
- de Rosnay, P., and J. Polcher, 1998, Modeling root water uptake in a complex land surface scheme coupled to a GCM, *Hydrology and Earth System Sciences*, *2*, 239–256, 1998.
- de Rosnay, P., J. Polcher, M. Bruen, and K. Laval, 2002, Impact of a physically based soil water flow and soil-plant interaction representation for modeling large scale land surface processes, *J. Geophys. Res.*, *107*, 10.1029/2001JD000634, 2002.
- Deardorff, J. W., 1966, The counter-gradient heat-flux in the lower atmosphere and in the laboratory, *J. Atmos. Sci.*, *23*, 503–506, 1966.
- Dufresne, J., and J. Grandpeix, Raccordement des modèles thermodynamiques de glace, d’océan et d’atmosphère, Note Interne 205, L.M.D., juin 1996.
- Dufresne, J.-L., P. Friedlingstein, M. Berthelot, L. Bopp, L. Fairhead, H. Le Treut, and P. Monfray, 2002, On the magnitude of positive feedback between future climate change and the carbon cycle, *Geophys. Res. Lett.*, *29*, 2002.
- Emanuel, K. A., and M. Zivkovic-Rothman, 1999, Development and evaluation of a convection scheme for use in climate models, *J. Atmos. Sci.*, *56*, 1766–1782, 1999.
- Emanuel, K. A., J. D. Neelin, and C. S. Bretherton, 1994, On large-scale circulations in convective atmospheres, *Q. J. R. Meteorol. Soc.*, *120*, 1111–1143, 1994.
- Emanuel, K. A., 1991, A scheme for representing cumulus convection in large-scale models, *J. Atmos. Sci.*, *48*, 2313–2335, 1991.
- Emanuel, K. A., 1993, A cumulus representation based on the episodic mixing model: the importance of mixing and microphysics in predicting humidity, *A.M.S. Meteorol. Monographs*, *24*, (46), 185–192, 1993.
- ERA-40 by ECMWF, 2002, ERA-40, forty-year european re-analysis of the global atmosphere, 2002, <http://www.ecmwf.int/products/data/archive/description>
- Farquhar, G., S. von Caemmerer, and J. Berry, 1980, A biochemical model of photosynthesis CO_2 fixation in leaves of C_3 species, *Planta*, *149*, 78–90, 1980.
- Forget, F., F. Hourdin, R. Fournier, C. Hourdin, O. Talagrand, M. Collins, S. R. Lewis, P. L. Read, and J.-P. Huot., 1999, Improved general circulation models of the Martian atmosphere from the surface to above 80 km, *J. Geophys. Res.*, *104*, 24,155–24,176, 1999.
- Fouquart, Y., and B. Bonnel, 1980, Computations of solar heating of the Earth’s atmosphere: A new parametrization, *Contrib. Atmos. Phys.*, *53*, 35–62, 1980.
- Genthon, C., G. Krinner, and E. Cosme, 2002, Free and laterally-nudged Antarctic climate of an Atmospheric General Circulation Model, *Monthly Weather Rev.*, *130*, 1601–1616, 2002.
- Grandpeix, J.-Y., V. Phillips, and R. Tailleux, 2005, Improved mixing representation in emanuel’s convection scheme, *Q. J. R. Meteorol. Soc.*, 2005, in press.
- Grenier, H., H. Le Treut, and T. Fichefet, 2000, Ocean-atmosphere interactions and climate drift in a coupled general circulation model, *Climate Dynamics*, *16*, 701–717, 2000.
- Guichard, F. a. J. P., J.-L. Redelsperger, P. Bechtold, J.-P. Chaboureaud, S. Cheinet, W. Grabowski, H. Grenier, C. Jones, M. Köhler, J.-M. Piriou, R. Tailleux, and M. Tomasini, 2004, Modelling the diurnal cycle of deep precipitating convection over land with cloud-resolving models and single-column models, *Q. J. R. Meteorol. Soc.*, *130*, (604C), 3139–3172, 2004.

- Harzallah, A., and R. Sadourny, 1994, Internal versus SST-forced atmospheric variability as simulated by atmospheric general circulation model, *J. Clim.*, *8*, 474–495, 1994.
- Hauglustaine, D. A., F. Hourdin, L. Jourdain, M.-A. Filiberti, S. Walters, J.-F. Lamarque, and E. A. Holland, 2004, Interactive chemistry in the Laboratoire de Météorologie Dynamique general circulation model: Description and background tropospheric chemistry evaluation, *J. Geophys. Res.*, *D18*, 4314–+, 2004.
- Hoskins, B. J., H. H. Hsu, I. N. James, M. Masutani, P. D. Sardeshmuck, and G. H. White, Diagnostics of the global atmospheric circulation based on ecmwf analysis 1979–1989, Technical document, WCRP/WMO, 1996.
- Hourdin, F., and A. Armengaud, 1999, Test of a hierarchy of finite-volume schemes for transport of trace species in an atmospheric general circulation model, *Mon. Wea. Rev.*, *127*, 822–837, 1999.
- Hourdin, F., and J.-P. Issartel, 2000, Sub-surface nuclear tests monitoring through the CTBT xenon network, *Geophys. Res. Lett.*, *27*, 2245–2248, 2000.
- Hourdin, F., P. Le Van, F. Forget, and O. Talagrand, 1993, Meteorological variability and the annual surface pressure cycle on Mars, *J. Atmos. Sci.*, *50*, 3625–3640, 1993.
- Hourdin, F., O. Talagrand, R. Sadourny, C. Régis, D. Gautier, and C. P. McKay, 1995, General circulation of the atmosphere of Titan, *Icarus*, *117*, 358–374, 1995.
- Hourdin, F., F. Couvreur, and L. Menut, 2002, Parameterisation of the dry convective boundary layer based on a mass flux representation of thermals, *J. Atmos. Sci.*, *59*, 1105–1123, 2002.
- Hourdin, F., S. Lebonnois, D. Luz, and P. Rannou, Titan’s stratospheric composition driven by condensation and dynamics, 2004.
- Jacquart, C., and E. Choissnel, 1995, Un modèle de bilan hydrique simplifié à deux réservoirs utilisable en agrométéorologie, *La Météorologie*, *8*, 4–17, 1995.
- James, I. N., 1989, The Antarctic drainage flow: implications for hemispheric flow on the Southern hemisphere, *Antarctic Science*, *1*, 279–290, 1989.
- Kasahara, A., Computational aspects of numerical models for weather prediction and climate simulation, in *Methods in computational physics*, edited by J. Chang, vol. 17, 1–66, Academic press, inc., 1977.
- King, J., and W. Connolley, 1997, Validation of the surface energy balance over the antarctic ice sheets in the uk meteorological office unified climate model, *J. Climate*, 1273–1287, 1997.
- Krinner, G., and C. Genthon, 1998, GCM simulations of the Last Glacial Maximum surface climate of Greenland and Antarctica, *Clim. Dyn.*, *14*, 741–758, 1998.
- Krinner, G., and C. Genthon, 2003, Tropospheric transport of continental tracers towards Antarctica under varying climatic conditions, *Tellus*, *53*, 54–70, 2003.
- Krinner, G., C. Genthon, Z.-X. Li, and P. Le Van, 1997, Studies of the Antarctic climate with a stretched-grid general circulation model, *J. Geophys. Res.*, *102*, 13731–13745, 1997.
- Krinner, G., J. Mangerud, M. Jakobsson, M. Crucifix, C. Ritz, and J. Svendsen, 2004, Enhanced ice sheet growth in Eurasia owing to adjacent ice dammed lakes, *Nature*, *427*, 429–432, 2004.
- Krinner, G., N. Viovy, N. de Noblet-Ducoudré, J. Ogée, J. Polcher, P. Friedlingstein, P. Ciais, S. Sitch, and C. Prentice, 2005, A dynamic global vegetation model for studies of the coupled atmosphere-biosphere system, *Glob. Biogeochem. Cyc.*, *19*, GB1015, 2005, doi:10.1029/2003GB002199.
- Kuo, H. L., 1965, On formation and intensification of tropical cyclones through latent heat release by cumulus convection., *J. Atmos. Sci.*, *22*, 40–63, 1965.
- Laval, K., R. Sadourny, and Y. Serafini, 1981, Land surface processes in a simplified general circulation model, *Geophys. Astrophys. Fluid Dyn.*, *17*, 129–150, 1981.
- Le Treut, H., and Z. X. Li, 1991, Sensitivity of an atmospheric general circulation model to prescribed SST changes: Feedback effects associated with the simulation of cloud optical properties., *Climate Dynamics*, *5*, 175–187, 1991.
- Le Treut, H., Z. Li, and M. Forichon, 1994, Sensitivity study of the lmd gcm to greenhouse forcing associated with two different cloud water parametrizations, *J. Clim.*, *7*, 1827–1841, 1994.
- Le Treut, H., M. Forichon, O. Boucher, and Z. Li, 1998, Sulfate Aerosol Indirect Effect and CO₂ Greenhouse Forcing: Equilibrium Response of the LMD GCM and Associated Cloud Feedbacks., *Journal of Climate*, *11*, 1673–1684, 1998.

- Levrard, B., F. Forget, F. Montmessin, and J. Laskar, 2004, Recent ice-rich deposits formed at high latitudes on Mars by sublimation of unstable equatorial ice during low obliquity, *Nature*, *431*, 1072–1075, 2004.
- Li, Z. X., and S. Conil, 2003, A 1000-year simulation with the IPSL ocean-atmosphere coupled model, *Annals of Geophysics*, *46(1)*, 39–46, 2003.
- Li, Z., 1999, Ensemble Atmospheric GCM Simulation of Climate Interannual Variability from 1979 to 1994., *Journal of Climate*, *12*, 986–1001, 1999.
- Lott, F., and M. Miller, 1997, A new sub-grid scale orographic drag parametrization: its formulation and testing., *Q. J. R. Meteorol. Soc.*, *123*, 101–128, 1997.
- Lott, F., 1999, Alleviation of stationary biases in a gem through a mountain drag parametrization scheme and a simple representation of mountain lift forces, *Monthly Weather Rev.*, *127*, 788–801, 1999.
- Louis, J.-F., 1979*a*, A parametric model of vertical eddy fluxes in the atmosphere., *Boundary-layer Meteorol.*, *17*, 187–202, 1979*a*.
- Louis, J.-F., 1979*b*, A parametric model of vertical eddy fluxes in the atmosphere., *Boundary-layer Meteorol.*, *17*, 187–202, 1979*b*.
- Manabe, S., J. S. Smagorinsky, and R. F. Strickler, 1965, Simulated climatology of a general circulation model with a hydrological cycle, *Mon. Wea. Rev.*, *93*, 769–798, 1965.
- Marti, O., P. Braconnot, J. Bellier, R. Benshila, S. Bony, P. Brockmann, P. Cadule, A. Caubel, S. Denvil, J.-L. Dufresne, L. Fairhead, M.-A. Filiberti, M.-A. Foujols, T. Fichet, P. Friedlingstein, J.-Y. Grandpeix, F. Hourdin, G. Krinner, C. Lévy, G. Madec, I. Musat, N. de Noblet, J. Polcher, and C. Talandier, The new IPSL climate system model: IPSL-CM4, Technical note, IPSL, available at <http://dods.ipsl.jussieu.fr/omamnce/IPSLCM4/DocIPSLCM4/models> of the shallow-water equations, *J. Atmos. Sci.*, *32*, 680–689, 1975*b*.
- Miller, M. J., A. C. M. Beljaars, and T. N. Palmer, 1992, The sensitivity of the ECMWF model to the parameterization of evaporation from the tropical oceans, *J. of Clim.*, *5*, 418–435, 1992.
- Morcrette, J. J., L. Smith, and Y. Fouquart, 1986, Pressure and temperature dependence of the absorption in longwave radiation parametrizations, *Contrib. Atmos. Phys.*, *59*, (4), 455–469, 1986.
- Myneni, R., S. Hoffman, J. Glassy, Y. Zhang, P. Votava, R. Nemani, S. Running, and J. Privette, 2002, Global products of vegetation leaf area and fraction absorbed PAR from year one of MODIS data, *Remote Sensing of Environment*, *83*, 214–231, 2002.
- Polcher, J., B. McAvaney, P. Viterbo, M.-A. Gaertner, A. Hahmann, J.-F. Mahfouf, J. Noilhan, T. Phillips, A. Pitman, C. Schlosser, J.-P. Schulz, B. Timbal, D. Verseghy, , and Y. Xue, 1998, A proposal for a general interface between land-surface schemes and general circulation models, *Global and Planetary Change*, *19*, 263–278, 1998.
- Poutou, E., G. Krinner, C. Genthon, and N. de Noblet-Ducoudré, 2004, Impact of soil freezing on future boreal climate change, *Clim. Dyn.*, *23*, 621–639, 2004.
- Quaas, J., O. Boucher, and F.-M. Bréon, 2004, Aerosol indirect effects in POLDER satellite data and the Laboratoire de Météorologie Dynamique-Zoom (LMDZ) general circulation model, *J. Geophys. Res.*, *109*, 2004.
- Quadrelli, R., and J. M. Wallace, 2004, A simplified linear framework for interpreting patterns of northern hemisphere wintertime climate variability, *J. Climate*, *17*, 3728–3744, 2004.
- Rannou, P., F. Hourdin, and C. P. McKay, 2002, A wind origin for Titan’s haze structure, *Nature*, *418*, 853–856, 2002.
- Sadourny, R., and K. Laval, January and July performance of the LMD general circulation model, in *New perspectives in Climate Modeling*, edited by A. Berger and C. Nicolis, Elsevier, 173–197, Amsterdam, 1984.
- Sadourny, R., 1975*a*, Compressible model flows on the sphere, *J. Atmos. Sci.*, *32*, 2103–2110, 1975*a*.
- Sadourny, R., 1975*b*, The dynamics of finite-difference models of the shallow-water equations, *J. Atmos. Sci.*, *32*, 680–689, 1975*b*.
- Sawyer, J. S., 1976, Observational characteristics of atmospheric fluctuations with a time scale of a month, *Q. J. R. Meteorol. Soc.*, *96*, 610–625, 1976.
- Shuman, C., R. Alley, S. Anandakrishnan, J. White, P. Grootes, and C. Stearns, 1995, Temperature and accumulation at the Greenland Summit: Comparison of high-resolution isotope profiles and satellite passive microwave brightness temperature trends, *J. Geophys. Res.*, *100*, 9165–9177, 1995.

Slingo, J. M., 1987, The development and verification of a cloud prediction scheme for the ecmwf model, *Q. J. R. Meteorol. Soc.*, *113*, (477), 899–927, 1987.

Smith, S. D., 1988, Coefficients for sea surface wind stress, heat flux, and wind profiles as a function of wind speed and temperature, *J. Geophys. Res.*, *93*, 15467–15472, 1988.

Taylor, K. E., D. Williamson, and F. Zwiers, The sea surface temperature and sea-ice concentration boundary conditions for AMIP II simulations, PCMDI Report No. 60 60, P.C.M.D.I., 2000.

Thompson, D. W. J., and J. M. Wallace, 1998, The Arctic Oscillation signature in the wintertime geopotential height and temperature fields, *Geophys. Res. Lett.*, *25*, 1297–1300, 1998.

Tiedtke, M., 1989, A comprehensive mass flux scheme for cumulus parameterization in large-scale models, *Mon. Wea. Rev.*, *117*, 1179–1800, 1989.

Van Leer, B., 1977, Towards the ultimate conservative difference scheme : IV. a new approach to numerical convection, *J. Computational Phys.*, *23*, 276–299, 1977.

Vaughan, D. G. and Bamber, J., M. Giovinetto, J. Russel, and A. Cooper, 1999, Reassessment of net surface mass balance in Antarctica, *J. Climate*, *12*, 933–946, 1999.

Vintzileos, A., P. Delecluse, and R. Sadourny, 1999, On the mechanisms in a tropical ocean-global atmosphere coupled general circulation model. Part I: mean state and the seasonal cycle, *Climate Dynamics*, *15*, 43–62, 1999.

Xie, P., and P. A. Arkin, 1997, A 17-year monthly analysis, based on gauge observations, satellite estimates, and, numerical model outputs, *Bull. Am. Meteorol. Soc.*, *78*, 2539–2558, 1997.

Xu, K.-M., and D. A. Randall, 1996*a*, Evaluation of statistically based cloudiness parameterisations used in climate models, *J. Atmos. Sci.*, *53*, 3103–3119, 1996*a*.

Xu, K.-M., and D. A. Randall, 1996*b*, A semiempirical cloudiness parameterisation for use in climate models, *J. Atmos. Sci.*, *53*, 3084–3102, 1996*b*.

Zhou, T. J., and Z. X. Li, 2002, Simulation of the east asian summer monsoon using a variable resolution atmospheric gcm, *Clim. Dyn.*, *19*, 167–180, 2002.

A Coupling between atmosphere and subsurfaces

Each atmospheric column has four types of subsurfaces: land, ocean, sea-ice, glacier. The coupling is the same whatever the subsurface model is. For instance, the coupling follows the same method if the SST is read or is computed by a full oceanic model or by a very simplified ocean (slab ocean). In our approach, the radiative code sees only one surface, with mean properties, and computes only one net flux in both shortwave and longwave domains. Only the turbulent fluxes (sensible, latent, momentum) are computed separately on each subsurface, and the tendency of the atmospheric column is the weighted sum of tendency computed by each subsurface.

The main goals of the new developments are the following:

- to redistribute the radiative fluxes, computed in the atmospheric column, on each subsurface taking into account the local properties of each subsurface
- to establish a clear interface between the atmospheric boundary layer code and the surface model, whatever it is.

An absolute requirement is energy and water conservation. In the following paragraphs, subscript i stands for a subsurface i of relative fraction w_i . For each atmospheric column, $\sum_i w_i = 1$.

A.1 Redistribution of the radiative fluxes

Shortwave flux The net shortwave flux at surface F_i^{sw} is first computed by the radiative code for the whole atmospheric columns with an albedo r

$$r = \sum_i w_i r_i \quad (8)$$

where r_i is the albedo of subsurface i . Assuming that the downward shortwave flux is the same above all the subsurfaces, the net shortwave flux F_i^{sw} for each subsurface i may be written as (Dufresne and Grandpeix, 1996):

$$F_i^{sw} = \frac{1 - r_i}{1 - r} F^{sw}. \quad (9)$$

One may verify that energy conservation is ensured (i.e. $\sum_i F_i^{sw} = F^{sw}$). This surface flux redistribution does not modify the flux at top of atmosphere and the heating of the atmosphere computed by the radiative code.

Longwave flux The net longwave flux at surface F^{lw} is computed by the radiative code for the whole atmospheric columns with an emissivity ϵ and a temperature T_r

$$\epsilon = \sum_i w_i \epsilon_i \quad \text{and} \quad T_r = \sum_i w_i \frac{\epsilon_i}{\epsilon} T_i \quad (10)$$

where ϵ_i is the emissivity of subsurface i and T_i is its temperature. Assuming that the downward longwave flux is the same above all the subsurfaces, the net longwave flux F_i^{lw} for each subsurface i reads (Dufresne and Grandpeix, 1996):

$$F_i^{lw} = \frac{\epsilon_i}{\epsilon} \left(F^{lw} + \frac{\partial F^{lw}}{\partial T_r} (T_i - T_r) \right) \quad (11)$$

with

$$\frac{\partial F^{lw}}{\partial T_r} = 4\epsilon\sigma T_r^3 \quad (12)$$

This surface flux redistribution does not modify the flux at top of atmosphere and the heating of the atmosphere computed by the radiative code.

A.2 Interface for coupling the turbulent fluxes

A first standard interface for the coupling between the surface and the atmosphere (Polcher et al., 1998) was proposed by the PILPS project. A drawback of the proposed approach is that solving of the turbulent fluxes in the boundary layer and solving of the temperature by the surface model are not completely separated. Indeed, the time evolution of the first atmospheric level variables (eq.(28) of Polcher et al. (1998)) is a function of the surface flux, but also of some surface coefficient. We overcome this difficulty by rewriting the discretised form of the vertical diffusion equation of the first atmospheric level and by considering explicitly the flux $F_{X,1/2}^{t+\delta t}$ between layer 1 and the surface:

$$\frac{X_1^t - X_1^{t+\delta t}}{\delta t} = \frac{1}{\delta z_1} \left(K_{X,3/2} \frac{X_2^{t+\delta t} - X_1^{t+\delta t}}{\delta z_{3/2}} - F_{X,1/2}^{t+\delta t} \right) \quad (13)$$

$$F_{X,1/2}^{t+\delta t} = K_{X,1/2} \frac{X_1^{t+\delta t} - X_0^{t+\delta t}}{\delta z_{1/2}} \quad (14)$$

Variables X stands for the dry static energy, the specific humidity or the wind speed; $K_{X,k-1/2}$ is the vertical diffusion coefficient for variable X at interface $k-1/2$ (between level k and $k-1$); δz_k is the thickness of layer k and $\delta z_{k-1/2}$ is the distance between the centers of layers k and $k-1$.

In the boundary layer To solve the vertical diffusion equation in the boundary layer, each variable of level k is written as a function of the variable of the level below $k-1$, for all levels except level 1:

$$X_k^{t+\delta t} = A_{X,k} X_{X,k-1}^{t+\delta t} + B_{X,k} \quad \text{for } k \geq 2 \quad (15)$$

For level 1, $X_2^{t+\delta t}$ may be suppressed from Eq. 13 using Eq. 15:

$$X_1^{t+\delta t} = A_{X,1} F_{X,1/2}^{t+\delta t} + B_{X,1} \quad (16)$$

with

$$A_{X,1} = -\frac{\delta t}{\delta z_1 C_{X,1}} \quad (17)$$

$$B_{X,1} = \left(X_1^t + \frac{\delta t K_{X,3/2}}{\delta z_1 \delta z_{3/2}} \right) \frac{1}{C_{X,1}} \quad (18)$$

$$C_{X,1} = 1 + \frac{\delta t K_{X,3/2}}{\delta z_1 \delta z_{3/2}} (1 - A_{X,2}) \quad (19)$$

One may verify that Eqs 16-19 make use only of the surface flux $F_{X,1/2}^{t+\delta t}$ and of atmospheric variables above layer 1. There is no use of surface variable or surface coefficient. For each variable X , variables X_1^t , $A_{X,1}$ and $B_{X,1}$ are transmitted by the boundary layer model to the surface model.

In the surface model The surface model has to compute the surface flux $F_{X,1/2}^{t+\delta t}$ for each variable X . For the temperature and the humidity at the surface, the new values $X_1^{t+\delta t}$ are computed (if required) through the energy and water budget of the surface. The coupling between atmosphere and surface being implicit, a relationship between $F_{X,1/2}^{t+\delta t}$ and $X_0^{t+\delta t}$ is required. This is obtained by combining Eq. 14 and Eq. 16:

$$F_{X,1/2}^{t+\delta t} = \frac{K_{X,1/2}}{\delta z_{1/2} - K_{X,1/2} A_{X,1}} (B_{X,1} - X_0^{t+\delta t}) \quad (20)$$

B About vertically integrated velocity potential

The purpose of this appendix is: (i) to express the vertical momentum of atmospheric columns in terms of the scalar potential of the horizontal wind; (ii) to derive from this expression an approximate formula for the scalar potential of this momentum. Only monthly mean velocity fields are considered and the scalar velocity potential at each level is chosen so that it is zero at the poles.

B.1 Vertical momentum

The vertical momentum \tilde{w} of atmospheric columns reads:

$$\tilde{w} = \int_{z_s}^{\infty} dz \rho w = - \int_{z_s}^{\infty} dz \frac{\omega}{g} \quad (21)$$

where w and ω are the vertical velocity expressed in z and pressure coordinates, respectively and z_s is the altitude of the surface.

Vertical integration of the continuity equation (taking into account $\vec{\nabla} \cdot \vec{V} = \nabla^2 \varphi$) yields an expression of ω in terms of the velocity potential:

$$\omega(z) - \omega_s = - \int_{z_s}^z dz' \nabla^2 \varphi(z') \rho(z') g \quad (22)$$

For monthly mean fields, the term $\omega_s = \frac{\partial p_s}{\partial t}$ is negligible. Then, substitution of (22) in (21) yields:

$$\tilde{w} = \int_0^{\infty} dz \int_{z_s}^z dz' \rho(z') \nabla^2 \varphi(z')$$

Let Z_0 be an altitude high enough so that $\omega(z_0) \simeq 0$. Then the integration may be limited to the triangle ($z < Z_0, z' < z$). Permuting the two integrations yields:

$$\begin{aligned} \tilde{w} &= \int_{z_s}^{Z_0} dz' \int_{z'}^{Z_0} dz \rho(z') \nabla^2 \varphi(z') \\ &= \int_{z_s}^{Z_0} dz' \rho(z') \nabla^2 \varphi(z') (Z_0 - z') \end{aligned} \quad (23)$$

The Z_0 term drops out since the vertical integral of $\nabla^2 \varphi$ is close to zero:

$$\tilde{w} = \frac{-1}{g} \int_{p_0}^{p_s} dp z_{(p)} \nabla^2 \varphi_{(p)} \quad (24)$$

B.2 Expressing the vertical momentum \tilde{w} in terms of the potential of the geopotential transport

We wish to express \tilde{w} as the Laplacian of some potential. In order to do this, one has to commute the Laplacian operator in formula (24) with the z term and with the integral operator.

We shall limit ourselves to the tropical band where the geopotential altitude has weak horizontal variations. With such an approximation, the Laplacian and the z term commute.

Now we want to commute the horizontal differentials with the vertical integration. Taking into account

the fact that the velocity is zero at the surface (so that $\vec{\nabla} \varphi(p_s) = 0$), one may write:

$$\begin{aligned} \frac{\partial}{\partial x} \left(\int_{p_0}^{p_s} dp z \varphi \right) &= \int_{p_0}^{p_s} dp z \frac{\partial \varphi}{\partial x} + z_{(p_s)} \varphi_{(p_s)} \frac{\partial p_s}{\partial x} \\ \frac{\partial^2}{\partial x^2} \left(\int_{p_0}^{p_s} dp z \varphi \right) &= \int_{p_0}^{p_s} dp z \frac{\partial^2 \varphi}{\partial x^2} + z_{(p_s)} \varphi_{(p_s)} \frac{\partial^2 p_s}{\partial x^2} \end{aligned} \quad (25)$$

Adding the analog formula for the y derivative, one gets:

$$\nabla^2 \left(\int_{p_0}^{p_s} dp z \varphi \right) = \int_{p_0}^{p_s} dp z \nabla^2 \varphi + z_{(p_s)} \varphi_{(p_s)} \nabla^2 p_s \quad (26)$$

Over oceans, the last rhs term is zero. Over continents, it is not necessarily zero, because of orography. However, with a spatial resolution of the order of 100 km, it stays several order of magnitude smaller than the first rhs term and we shall neglect it.

Then, one may write the vertical momentum \tilde{w} as the Laplacian of a function $\tilde{\varphi}$:

$$\begin{cases} \tilde{w} \simeq \frac{-1}{g} \nabla^2 \tilde{\varphi} \\ \tilde{\varphi} = \int_{p_0}^{p_s} dp z \varphi \end{cases} \quad (27)$$

Finally, using the same technique and the same approximations one may prove that $\tilde{\varphi}$ is close to the saclar potential of the horizontal transport \vec{G} of geopotential:

$$\begin{aligned} \vec{G} &= \int_0^{\infty} dz \rho \vec{V} g z \\ &= \int_0^{p_s} dp z \vec{V} \end{aligned} \quad (28)$$

As an illustration, Fig. 19 displays the potential $\tilde{\varphi}$ of the annual mean geopotential transport and the mean vertical velocity. The similarity of $\tilde{\varphi}$ and ω_{500} is obvious. However, $\tilde{\varphi}$ is smoother than ω_{500} and might be a better indicator of dynamic regimes. Finally, the lowest pannel illustrates the strong link between large scale ascent and precipitation.

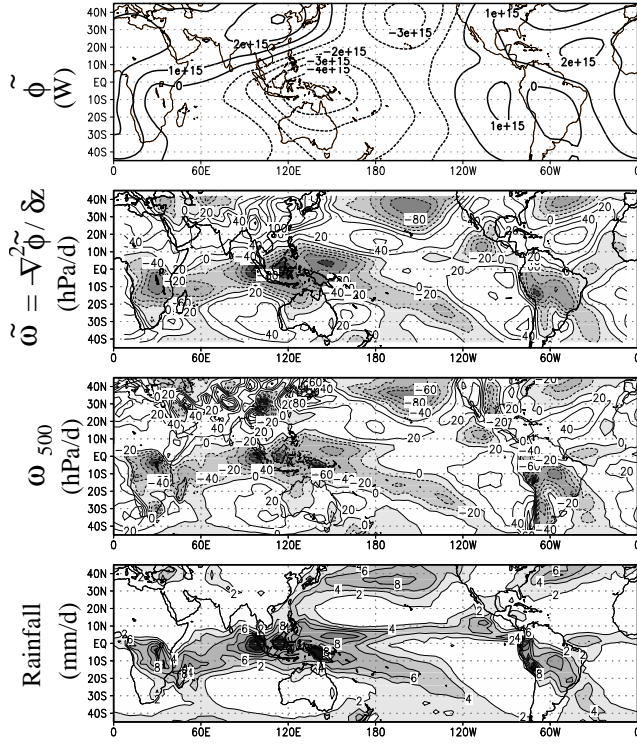


Figure 19: Potential $\tilde{\varphi}$ of the annual mean of the horizontal transport of geopotential (upper panel) and mean vertical velocity $\bar{\omega} = \frac{1}{Z_0 - z_s} \int_{z_s}^{Z_0} dz \omega = \frac{1}{Z_0 - z_s} \nabla^2 \tilde{\varphi}$ (with $Z_0 - z_s = 15$ km) (second panel) for one of the AMIP simulations; to be compared with ω_{500} and annual precipitation (two lower panels).